A STABLE SPH DISCRETIZATION OF THE ELLIPTIC OPERATOR WITH HETEROGENEOUS COEFFICIENTS

ALEXANDER A. LUKYANOV† AND KEES VUIK†

ABSTRACT. Smoothed particle hydrodynamics (SPH) has been extensively used to model high and low Reynolds number flows, free surface flows and collapse of dams, study pore-scale flow and dispersion, elasticity, and thermal problems. In different applications, it is required to have a stable and accurate discretization of the elliptic operator with homogeneous and heterogeneous coefficients. In this paper, the stability and approximation analysis of different SPH discretization schemes (traditional and new) of the diagonal elliptic operator for homogeneous and heterogeneous media are presented. The optimum and new discretization scheme is also proposed. This scheme enhances the Laplace approximation (Brookshaw's scheme [1] and Schwaiger's scheme [2]) used in the SPH community for thermal, viscous, and pressure projection problems with an isotropic elliptic operator. The numerical results are illustrated by numerical examples, where the comparison between different versions of the meshless discretization methods are presented.

1. INTRODUCTION

Smoothed particle hydrodynamics (SPH) was developed a few decades ago to model inviscid fluid and gas flow dynamics in astrophysical problems [3–6]. The SPH is an interpolation-based numerical technique that can be used to solve systems of partial differential equations (PDEs) using either Lagrangian or Eulerian descriptions. The nature of SPH method allows to incorporate different physical and chemical effects into the discretized governing equations with relatively small code-development effort. In addition, geometrically complex and/or dynamic boundaries, and interfaces can be handled without undue difficulty. The SPH numerical procedure of calculating state variables (i.e., density, velocity, and gradient of deformation) are computed as a weighted average of values in a local region. Despite a few advantages of SPH method, this method is not free from disadvantages. For example, for fluids, gases, or solids with non-trivial boundaries there is incompleteness of the kernel support combined with the lack of consistency of the kernel interpolation in conventional meshless methods which results in fuzzy boundaries. In some cases, this can be fixed by an automatic incorporation of the boundary condition [3]. The completeness of mesh free particle methods was discussed in [7]. However, care must be taken to ensure that variables whose values do not approach zero at boundaries are accurately represented.

It has been observed in the literature that meshless methods (e.g., SPH) are not free from instabilities, especially in the modeling solid mechanics problems. For example, the tensile instabilities

were identified in [8] by performing the Neumann analysis of the one-dimensional governing equations (conservation laws). Therefore, different stabilization techniques have been developed. It is important to note at this point that it is very difficult to perform the general Neumann analysis in two- and three-dimensions. Furthermore, the high-frequency instability results from the low order discretization (rank deficient) of the divergence operator. The tensile instability results from the interaction between the second derivative of the Eulerian kernel (i.e., computed kernel in the Eulerian coordinates) and the tensile stress. The tensile instability only occurs for the Eulerian kernels because the Eulerian kernels depend on both the stress and the second derivative of the kernel. It has been shown [9] that in the case where the kernel is a function of the Lagrangian coordinates (the Lagrangian kernel), tensile instability does not occur. A comprehensive analysis on this subject can be found in [9]. Recently, some regularization and stabilization of SPH schemes were proposed in [10], [11].

Since its introduction, SPH has been successfully used to model a wide range of fluid flows and the behavior of solids subjected to large deformations. For example, the SPH method was applied to simulate high energy explosions [12] and impact [13, 14], most notably free surface flows and collapse of dams [15], elastoplasticity [14, 16–18], to model low Reynolds number flows [19, 20], to study pore-scale flow and dispersion [21, 22], and for thermal problems [2, 17, 23].

In different applications including, but not limited to, fluid flow related problems, it is required to have the stable and accurate discretization of the following operator (diagonal elliptic operator), which is the research subject of this paper:

$$\mathbf{L}\left(\mathbf{u}\right) = -\nabla\left(\mathbf{M}\left(\boldsymbol{r}\right)\nabla\mathbf{u}\left(\boldsymbol{r}\right)\right) - g\left(\boldsymbol{r}\right),\ \forall \boldsymbol{r} \in \Omega \subset \mathbb{R}^n,$$
$$\mathbf{M}\left(\boldsymbol{r}\right) \in \{\mathrm{diag}[m(\boldsymbol{r})] : m(\boldsymbol{r}) \in \mathbb{R}^n_+,\ m\left(\boldsymbol{r}\right) \in L_2\left(\Omega\right)\},\ \mathrm{diag} : \mathbb{R}^n \to \mathbb{R}^{n \times n},$$

(1)

where $\mathbf{u}\left(\boldsymbol{r}\right)$ is the unknown scalar or vector variable field, $\mathbf{M}^{\alpha\beta}\left(\boldsymbol{r}\right)$ is the diagonal matrix of the mobility field, e.g., one example includes $\mathbf{M}^{\alpha\beta}\left(\boldsymbol{r}\right) = m\left(\boldsymbol{r}\right)\delta_{\alpha\beta},\ \alpha,\beta = 1,\ldots,n;$, where $m\left(\boldsymbol{r}\right)$ is the mobility scalar field, $\delta_{\alpha\beta}$ is the Kronecker symbol, $n = 1, 2, 3$ is the spatial dimension. The sink/source term $g\left(\boldsymbol{r}\right)$ is assumed to be zero in this paper. Consider the operator in the expression (1) with piecewise continuous coefficients $\mathbf{M}\left(\boldsymbol{r}\right)$ in Ω. It has been noticed that some of the numerical methods for elliptic equations may violate the maximum principle (i.e. lead to spurious oscillations). Therefore, proposed methods must satisfy a discrete maximum principle to avoid any spurious oscillations. This is also applicable to meshless discretizations. Usually, the oscillations are closely related to the poor approximation of the variable gradient $\nabla\mathbf{u}$ in the flux computation. In this paper, different numerical discretizations of the elliptic isotropic operator are analyzed. The objective of this paper is to develop numerical scheme satisfying the two-point flux approximation nature in the form

$$\mathbf{L}\left(\mathbf{u}\right) \approx \sum_J V_{\boldsymbol{r}_J}\Psi\left(\left[\mathbf{u}\left(\boldsymbol{r}_J\right) - \mathbf{u}\left(\boldsymbol{r}_I\right)\right], \boldsymbol{r}_J - \boldsymbol{r}_I\right) - g\left(\boldsymbol{r}_I\right),$$

(2)

where J is the neighboring particle of the particle I, $V_{\boldsymbol{r}_J}$ is the J - particle volume, Ψ is the special kernel. This structure (2) allows to have a better analysis of the stability and monotonicity. Furthermore, this will allow to apply upwinding strategy during the solution of nonlinear PDEs. The optimum discretization scheme of the shape (2) is proposed in this paper. This scheme is based both on the Laplace approximation (Brookshaw's scheme [1]) and on a gradient approximation commonly used in the SPH community for thermal, viscous, and pressure projection problems. The proposed discretization scheme is combined with mixed corrections, which ensure linear completeness. The mixed correction utilizes Shepard Functions in combination with a correction to

derivative approximations. In corrected meshless methods, the domain boundaries and field variables at the boundaries are approximated with the improved accuracy comparing to the conventional SPH method. The resulting new scheme improves the particle deficiency (kernel support incompleteness) problem. The outline of the paper is as follows. In section 2, the existing discretizations of the Laplace operator with the building blocks necessary for these methods are discussed. In this section, the SPH kernel and its gradient properties are also discussed. The description of meshless transmisibilities and their connections to the existing mesh-dependent discretization schemes is given in section 3 including the construction of a new meshless discretization scheme. The approximation, stability, and monotonicity analysis are performed in section 4. The numerical analysis of different boundary value problems is presented in section 5. The paper is concluded by section 6.

2. SPH DISCRETIZATION OF THE LAPLACE OPERATOR

The meshless approximations (SPH approximations) to the operator (1) with heterogeneous and homogeneous coefficients are presented in this section. Let us consider a rectangle in $\mathbb{R}^n$, $n = 1, 2, 3$:

$$\Omega = \{\boldsymbol{r} = \{x_i\} \in \mathbb{R}^n \mid \quad 0 < |x_i - a_i| < l_i, \ l_i \in \mathbb{R}_+, \quad \forall i = 1, \ldots, n\} \tag{3}$$

as the numerical domain. Here, a_i are the center coordinates of the rectangular and l_i are the side lengths. The following norms are used to quantify the accuracy of different approximations for the entire numerical domain Ω:

$$\|\mathbf{f}\|_{\bar{\Omega}}^p = \left(\sum_{\boldsymbol{\xi}_k \in \bar{\Omega}} V_{\boldsymbol{\xi}_k} \left(|\mathbf{f}|\right)^p \right)^{\frac{1}{p}}, \ \|\mathbf{f}\|_{\tilde{\Omega}}^p = \left(\sum_{\boldsymbol{\xi}_k \in \tilde{\Omega}} V_{\boldsymbol{\xi}_k} \left(|\mathbf{f}|\right)^p \right)^{\frac{1}{p}} \tag{4}$$

where $\mathbf{f}$ is the approximated physical quantity, $V_{\boldsymbol{\xi}_k}$ is the volume of the particle $\boldsymbol{\xi}_k$, $\bar{\Omega}$ denotes entire domain including boundary particles, $\tilde{\Omega}$ denotes only internal part of the domain Ω.

The proposed discretization schemes should be compatible with a discontinuous $m(\boldsymbol{r})$ (or piecewise function) coefficient of the operator (1) since this coefficient cannot be differentiable in the classical sense. The standard SPH spatial discretization of the Laplace operator (1) arises from the following relations $(g(\boldsymbol{r}) = 0, \ \forall \boldsymbol{r})$:

$$\langle \mathbf{L}\left(\mathbf{u}\left(\boldsymbol{r}_I\right)\right)\rangle = \lim_{\tilde{h}_I \to 0} \int_{\Omega_{\boldsymbol{r}_I, \tilde{h}_I}} \mathbf{L}\left(\mathbf{u}\left(\boldsymbol{r}\right)\right) W\left(\boldsymbol{r} - \boldsymbol{r}_I, \tilde{h}_I\right) dV_{\boldsymbol{r}} \approx$$

$$\approx \lim_{\tilde{h}_I \to 0} \left[\int_{\Omega_{\boldsymbol{r}_I, \tilde{h}_I}} \mathbf{M}\left(\boldsymbol{r}\right) \nabla \mathbf{u}\left(\boldsymbol{r}\right) \cdot \nabla W\left(\boldsymbol{r} - \boldsymbol{r}_I, \tilde{h}_I\right) dV_{\boldsymbol{r}} \right], \tag{5}$$

where $W\left(\boldsymbol{r} - \boldsymbol{r}_I, \tilde{h}_I\right)$ is the kernel that weakly approximates the Dirac delta function $\delta\left(\boldsymbol{r} - \boldsymbol{r}_I\right)$ but with finite characteristic width $\tilde{h}_I$ around the particle I. The effective characteristic width $\tilde{h}_I$ will be defined in the upcoming section using real smoothing particle length h_I. However, it is important to note that, in the case of the homogeneous particle distribution, it is common to use $\tilde{h}_I = f \cdot h_p$, $f \geq 1$, where h_p is the inter-particles distance. Hence, it is important that $\tilde{h}_I$ and h_p are not mixed up during the analysis. The control volumes in the meshless discretization are the patches, which are interior to the support of the kernels $W\left(\boldsymbol{r} - \boldsymbol{r}_I, \tilde{h}_I\right)$, i.e. $\Omega_{\boldsymbol{r}_I, \tilde{h}_I} = \operatorname{supp} W\left(\boldsymbol{r} - \boldsymbol{r}_I, \tilde{h}_I\right)$, $\tilde{h}_I$ is the diameter (or smoothing length) of the particle I, and $\boldsymbol{r}$, $\boldsymbol{r}_I$ are points in Euclidean

space $\mathbb{R}^n$. Additionally, it can be required that the kernels are radially symmetric and compactly supported (supp W) as:

$$\Omega_{\boldsymbol{r}_I, \tilde{h}_I} = \text{supp } W = \{\mathbf{r}_J \mid W(\boldsymbol{r}_J - \boldsymbol{r}_I, \tilde{h}_{IJ}) \neq 0\}, \tag{6}$$

where $\tilde{h}_{IJ}$ is the effective smoothing length between particles located at $\boldsymbol{r}_I$ and $\boldsymbol{r}_J$, which will be defined in the upcoming section. From the definition of the $\Omega_{\boldsymbol{r}_I, \tilde{h}_I}$, it follows that there is an infinite cover of the numerical domain Ω:

$$\Omega = \bigcup_{\boldsymbol{r}_I \in \Omega} \Omega_{\boldsymbol{r}_I, \tilde{h}_I}. \tag{7}$$

According to the Heine-Borel theorem, there is a finite subcover (since we consider only compact numerical domain Ω), that is

$$\Omega = \text{span} \left\{ \Omega_{\boldsymbol{r}_I, \tilde{h}_I} / I = 1, ..., N \right\}, \tag{8}$$

where N is the number of particles in the numerical discretization. The SPH spatial discretization of the integral (5) is defined over the control volumes $\Omega_{\boldsymbol{r}_I, \tilde{h}_I}$ to obtain the final discretization of the Laplace operator. The final step in the particle method is to approximate the integral relation on the right-hand side of the (5) using Monte-Carlo expressions or any cubature rules [7, 17, 24, 25] and which is known as the particle approximation step.

The assumption that the boundary term from the integration by parts is zero in (5) is valid only in regions where the kernel has a full support, or the function, or the gradient of the function itself is zero. For particles near free surfaces or boundary, the neglect of these terms leads to significant errors for boundary value problems. Several techniques have been developed to address these errors through various correction methods, e.g., by calculating the boundary integrals [25]. In addition, this can be corrected as it will be shown below by applying normalized corrected meshless methods in the derivative approximations. In the following section, the commonly used SPH kernels and its gradients are considered.

2.1. **SPH kernel and its gradient.** A central point of the SPH formalism is the concept of the interpolating function (or kernel) through which the continuum properties of the medium are recovered from a discrete sample of N points (7) with prescribed mass m_I (for conventional Lagrangian methods) or volume V_I (for fully Eulerian methods). In the Lagrangian formulation, these points move according to the specified governing laws, whereas these points are fixed in space for the Eulerian formulation. A good interpolating kernel must satisfy a few basic requirements: it must weakly tend to the delta function in the continuum limit and has to be a continuous function with piecewise first derivatives at least. From a more practical point of view it is also advisable to deal with symmetric finite range kernels, the latter to avoid N^2 calculations. Cubic and quintic splines are the commonly used kernels in SPH formulations [25, 26]. Since the quintic spline does not provide the numerical advantages, the cubic spline is used in this paper:

$$W(z, \tilde{h}) = \frac{\Xi}{\tilde{h}^D} \begin{cases} 1 - \dfrac{3}{2}z^2 + \dfrac{3}{4}z^3, & 0 \leqslant z \leqslant 1; \\ \dfrac{1}{4}(2 - z)^3, & 1 \leqslant z \leqslant 2; \\ 0, & z > 2; \end{cases} \tag{9}$$

where $z = \|\boldsymbol{r}_J - \boldsymbol{r}_I\|_2 / \tilde{h}$ is the dimensionless variable, $\tilde{h} = \tilde{h}_{IJ}$ is the effective smoothing length between particles I and J, and Ξ is the normalization factor equal to $3/2$, $10/(7\pi)$, and $1/\pi$ in 1D,

2D, and 3D, respectively. The different choices of computing effective smoothing length between particles used in this paper will be discussed in the upcoming subsection.

Although, the kernel is normalized in continuous sense, it is important to note that $W\left(\mathbf{r}_J - \mathbf{r}_I, \tilde{h}_{IJ}\right)$ does not satisfy the normalization condition in the discrete space

$$\sum_{\mathbf{r}_J \in \Omega_{\mathbf{r}_I, \tilde{h}_I}} W\left(\mathbf{r}_J - \mathbf{r}_I, \tilde{h}_{IJ}\right) V_{\mathbf{r}_J} \neq 1$$

due to the particle distribution and incomplete kernel support near the boundary and, hence, the discretized-normalized kernel function can be considered:

$$\overline{W}\left(\boldsymbol{r}_J - \boldsymbol{r}_I, \tilde{h}_{IJ}\right) =$$

$$= \frac{W\left(\boldsymbol{r}_J - \boldsymbol{r}_I, \tilde{h}_{IJ}\right)}{\displaystyle\sum_{\boldsymbol{r}_J \in \Omega_{\boldsymbol{r}_I, \tilde{h}_I}} W\left(\boldsymbol{r}_J - \boldsymbol{r}_I, \tilde{h}_{IJ}\right) V_{\boldsymbol{r}_J}} = \frac{W\left(\boldsymbol{r}_J - \boldsymbol{r}_I, \tilde{h}_{IJ}\right)}{\nu\left(\boldsymbol{r}_I\right)} \tag{10}$$

where $\nu\left(\boldsymbol{r}_I\right)$ is the specific volume of particle $\boldsymbol{r}_I$ (i.e., it is approximately the inverse of the particle volume) which has a larger value in a dense particle region than in a dilute particle region. In regions of the high particle density, the denominator in (10) is high resulting in lower values of the kernel $\overline{W}\left(\boldsymbol{r}_J - \boldsymbol{r}_I, \tilde{h}_{IJ}\right)$. Thus the denominator normalizes the kernel function to ensure that the kernel $\overline{W}\left(\boldsymbol{r}_J - \boldsymbol{r}_I, \tilde{h}_{IJ}\right)$ forms a local partitioning of unity

$$\sum_{\boldsymbol{r}_J \in \Omega_{\boldsymbol{r}_I, \tilde{h}_I}} \overline{W}\left(\boldsymbol{r}_J - \boldsymbol{r}_I, \tilde{h}_{IJ}\right) V_{\boldsymbol{r}_J} = 1 \tag{11}$$

regardless of the particle distribution within the $\Omega_{\boldsymbol{r}_I, \tilde{h}_I} = \operatorname{supp} W\left(\boldsymbol{r} - \boldsymbol{r}_I, \tilde{h}_I\right)$. The discretized-normalized kernel function $\overline{W}\left(\boldsymbol{r} - \boldsymbol{r}_I, \tilde{h}\right)$ will also be used in the discretization schemes below. At this point, all possible options of computing $\overline{\nabla W}(\boldsymbol{r}_J - \boldsymbol{r}_I, \tilde{h}_{IJ})$ are listed:

$$\overline{\nabla W}(\boldsymbol{r}_J - \boldsymbol{r}_I, \tilde{h}_{IJ}) = \nabla_{\boldsymbol{r}_J} W(\boldsymbol{r}_J - \boldsymbol{r}_I, \tilde{h}_{IJ}) = -\nabla_{\boldsymbol{r}_I} W(\boldsymbol{r}_J - \boldsymbol{r}_I, \tilde{h}_{IJ}), \tag{12}$$

$$\overline{\nabla W}(\boldsymbol{r}_J - \boldsymbol{r}_I, \tilde{h}_{IJ}) = \nabla_{\boldsymbol{r}_I} \overline{W}(\boldsymbol{r}_J - \boldsymbol{r}_I, \tilde{h}_{IJ}) =$$

$$= \frac{\nabla_{\boldsymbol{r}_I} W(\boldsymbol{r}_J - \boldsymbol{r}_I, \tilde{h}_{IJ})}{\nu(\boldsymbol{r}_I)} - \frac{W(\boldsymbol{r}_J - \boldsymbol{r}_I, \tilde{h}_{IJ}) \nabla_{\boldsymbol{r}_I} \nu(\boldsymbol{r}_I)}{\nu^2(\boldsymbol{r}_I)},$$

$$\nabla_{\boldsymbol{r}_I} \nu(\boldsymbol{r}_I) = \sum_{\boldsymbol{r}_J \in \Omega_{\boldsymbol{r}_I, \tilde{h}_I}} \nabla_{\boldsymbol{r}_I} W(\boldsymbol{r}_J - \boldsymbol{r}_I, \tilde{h}_{IJ}) V_{\boldsymbol{r}} \tag{13}$$

where $\nu(\boldsymbol{r}_I)$ is the specific volume of the particle located at the point $\boldsymbol{r}_I$. Additionally two options can be written as

$$\overline{\nabla W}(\boldsymbol{r}_J - \boldsymbol{r}_I, \tilde{h}_{IJ}) = \widetilde{\nabla}_{\boldsymbol{r}_J} \overline{W}(\boldsymbol{r}_J - \boldsymbol{r}_I, \tilde{h}_{IJ}) = \frac{\nabla_{\boldsymbol{r}_J} W(\boldsymbol{r}_J - \boldsymbol{r}_I, \tilde{h}_{IJ})}{\nu(\boldsymbol{r}_I)} \tag{14}$$

where $\nu(\boldsymbol{r}_I)$ is assumed to be a constant during the differentiation with respect to $\boldsymbol{r}_J$ and the alternative case is when

$$\nu(\boldsymbol{r}_I, \boldsymbol{r}_J) = \sum_{\boldsymbol{r}_J \in \Omega_{\boldsymbol{r}_I, \tilde{h}_I}} W(\boldsymbol{r}_J - \boldsymbol{r}_I, \tilde{h}_{IJ}) V_{\boldsymbol{r}_J},$$

leading to the following relations

$$\overline{\nabla W}(\boldsymbol{r}_J - \boldsymbol{r}_I, \tilde{h}_{IJ}) = \overline{\nabla}_{\boldsymbol{r}_J} \overline{W}(\boldsymbol{r}_J - \boldsymbol{r}_I, \tilde{h}_{IJ}) =$$
$$= \frac{\nabla_{\boldsymbol{r}_J} W(\boldsymbol{r}_J - \boldsymbol{r}_I, \tilde{h}_{IJ})}{\nu(\boldsymbol{r}_I, \boldsymbol{r}_J)} - \frac{W(\boldsymbol{r}_J - \boldsymbol{r}_I, \tilde{h}_{IJ}) \nabla_{\boldsymbol{r}_J} \nu(\boldsymbol{r}_I, \boldsymbol{r}_J)}{\nu^2(\boldsymbol{r}_I, \boldsymbol{r}_J)}, \quad . \tag{15}$$
$$\nabla_{\boldsymbol{r}_J} \nu(\boldsymbol{r}_I, \boldsymbol{r}_J) = \nabla_{\boldsymbol{r}_J} W(\boldsymbol{r}_J - \boldsymbol{r}_I, \tilde{h}_{IJ}) V_{\boldsymbol{r}_J}$$

Where $\nabla_{\boldsymbol{r}_J}$ denotes nabla operator with respect to $\boldsymbol{r}_J$ and this index is omitted throughout this paper starting from here.

Similar to the MLS method [27], equations (13) and (15) are two different forms of "full derivatives". At the same time, equations (12) and (14) are two different forms of "diffuse derivatives". From these options, it follows that "full derivatives" are connected with the differentiation of a discrete function and "diffuse derivatives" are connected with the differentiation of an exact function. Both types of derivatives have some advantages and disadvantages and the choice depends on the application. The impact of different options on numerical results will be shown below. The SPH method shows good approximation properties in regions where the kernel has full support. For particles near free surfaces or boundaries, the SPH method shows a poor approximation. Several techniques have been developed to address these errors through various correction methods, e.g., by applying normalized - corrected meshless methods in the derivative approximations [7,13,14,25], which requires normalized - corrected definitions of the kernel gradient as follows:

$$\overline{\nabla_\alpha^* W} = \mathbf{C}_{\alpha\beta} \overline{\nabla_\beta W}, \tag{16}$$

$$\mathbf{C}_{\alpha\beta} = \left[\sum_{\boldsymbol{r}_J \in \Omega_{\boldsymbol{r}_I, \tilde{h}_I}} V_{\boldsymbol{r}_J} \left[\boldsymbol{r}_J^\alpha - \boldsymbol{r}_I^\alpha \right] \overline{\nabla_\beta W} \left(\boldsymbol{r}_J - \boldsymbol{r}_I \right) \right]^{-1}, \tag{17}$$

$$\sum_{\Omega_{\boldsymbol{r}_I, h}} V_{\boldsymbol{r}_J} \left[\boldsymbol{r}_J^\gamma - \boldsymbol{r}_I^\gamma \right] \overline{\nabla_\alpha^* W} \left(\boldsymbol{r}_J - \boldsymbol{r}_I, h \right) = \delta_{\gamma\alpha}, \quad \forall \gamma, \alpha; \tag{18}$$

where the summation by repeating indexes is assumed throughout this paper, $\overline{\nabla_\alpha^* W}$ is the normalized-corrected gradient of the kernel, and $\mathbf{C}_{\alpha\beta}$ is the correction symmetric tensor [28]. It was shown that the value of the minimum eigenvalue $\lambda^{\mathbf{C}}(\boldsymbol{r}_I)$ of the matrix $\mathbf{C}^{-1}$ based on the discretized-normalized kernel function depends on the particle distribution within the domain $\Omega_{\boldsymbol{r}_I, \tilde{h}_I} = \text{supp} W \left(\boldsymbol{r} - \boldsymbol{r}_I, \tilde{h}_I \right)$. When going away from the $\Omega_{\boldsymbol{r}_I, \tilde{h}_I}$ domain this eigenvalue tends theoretically to zero, while inside this domain the eigenvalue tends theoretically to one. This important information allows determining regions of the continuum media where free-surfaces are located [29].

In this paper, the discretizations of the Laplace operator are based on the gradient of the kernel. Several methods of Laplace discretizations were proposed [30–33] using second derivatives of the variable $\mathbf{u}$. However, second-order derivatives can often be avoided entirely if the PDE is written in a weak form. It is important to note that approximations using second-order derivatives of the

kernel are often noisy and sensitive to the particle distribution, particularly for spline kernels of lower orders.

2.2. **SPH symmetrization of smoothing length.** The true particle smoothing length $\tilde{h}_I$ may vary both in space and time in general. Therefore, in general case, each particle has its own smoothing length $\tilde{h}_I$. Considering the case where $\tilde{h}_I \neq \tilde{h}_J$ for two different interacting particles I and J and the kernel support based on $\tilde{h}_I$ and located in I which covers the particle J but the kernel support located in J does not cover the particle I. In this case, the particle I acting on particle J (produces, e.g., a flux or a force) without particle J acting on the particle I, which leads to a violation of fundamental laws (e.g., mass conservation or Newton's third law) for a closed system of particles. This problem has been resolved by introducing the symmetrization of the smoothing length. In this study, the following symmetrization option is used:

$$\tilde{h}_{IJ} = \frac{\tilde{h}_I + \tilde{h}_J}{2}. \tag{19}$$

In addition, it is clear that $\tilde{h}_I$ has to be defined as

$$\tilde{h}_I = \sup_{J:\boldsymbol{r}_j \in \Omega_{\boldsymbol{r}_I, \tilde{h}_I}} \tilde{h}_{IJ}. \tag{20}$$

This completes the description of basic properties of SPH method allowing to construct all necessary building elements of SPH discretization such as list of neighbors, kernel values, and kernel gradients. The following sections describe the traditional and newly proposed discretization schemes for the Laplace operator.

2.3. **Brookshaw's scheme (1985).** Brookshaw proposed [1] an approximation of the Laplacian for an inhomogeneous scalar field $m(\boldsymbol{r})$, i.e., $\mathbf{M}^{\alpha\beta}(\boldsymbol{r}) = m(\boldsymbol{r})\delta_{\alpha\beta}$, $\alpha, \beta = 1, \ldots, n$; that only includes first order derivatives:

$$-\langle \nabla (m(\boldsymbol{r}_I)\nabla \mathbf{u}(\boldsymbol{r}_I)) \rangle =$$

$$\sum_{\Omega_{\boldsymbol{r}_I, \tilde{h}_I}} V_{\boldsymbol{r}_J} [\mathbf{u}(\boldsymbol{r}_J) - \mathbf{u}(\boldsymbol{r}_I)] \frac{(\boldsymbol{r}_J - \boldsymbol{r}_I) \cdot (m_J + m_I)\overline{\nabla W}\left(\boldsymbol{r}_J - \boldsymbol{r}_I, \tilde{h}_{IJ}\right)}{\|\boldsymbol{r}_J - \boldsymbol{r}_I\|^2}, \tag{21}$$

where $V_{\boldsymbol{r}_J}$ is the volume of the particle J, $\|\bullet\|$ is the Euclidean norm throughout this paper, $\mathbf{u}(\boldsymbol{r})$ is the unknown scalar or vector field (e.g., pressure p or velocity $\boldsymbol{v}$) $\forall \boldsymbol{r} \in \Omega \subset \mathbb{R}^n$, $m_I = m(\boldsymbol{r}_I)$, $\boldsymbol{r}_I \in \Omega \subset \mathbb{R}^n$ and $m_J = m(\boldsymbol{r}_J)$, $\boldsymbol{r}_J \in \Omega \subset \mathbb{R}^n$ are the field coefficients.

This scheme can be derived by applying the particle approximation step to the right-hand side of (5) with the following assumptions

$$\nabla \mathbf{u}(\boldsymbol{r}_J) \approx [\mathbf{u}(\boldsymbol{r}_J) - \mathbf{u}(\boldsymbol{r}_I)] \frac{(\boldsymbol{r}_J - \boldsymbol{r}_I)}{\|\boldsymbol{r}_J - \boldsymbol{r}_I\|^2}. \tag{22}$$

Some special words need to be said about the mobility approximation, which comes in the form

$$2m(\boldsymbol{r}_J) \approx m_J + m_I. \tag{23}$$

The factor 2 is introduced to compensate the factor of $1/2$ in the second leading term of the Taylor expansion of the relation (22). Furthermore, the relation (23) allows to capture a heterogeneous mobility field distribution.

The discretization scheme (21) is at least $\mathcal{O}\left(h^{\omega}\right)$, $0 \leq \omega < 2$, $h = \sup\limits_{I:\boldsymbol{r}_I \in \Omega} \tilde{h}_I$ order of accuracy in average for any scalar mobility field $m\left(\boldsymbol{r}\right) \in C^1\left(\Omega\right)$, $m\left(\boldsymbol{r}\right) \geq 0$ everywhere within the numerical domain Ω sufficiently far away from the boundary $\partial\Omega$. Using Taylor series expansions about a point $\boldsymbol{r}_I$, the following relations can be written:

$$\mathbf{u}\left(\boldsymbol{r}_J\right) = \mathbf{u}\left(\boldsymbol{r}_I\right) + \mathbf{u}_{,\alpha}\left(\boldsymbol{r}_I\right)\left[r_J^{\alpha} - r_I^{\alpha}\right] + \frac{1}{2}\mathbf{u}_{,\alpha\gamma}\left(\boldsymbol{r}_I\right)\left[r_J^{\alpha} - r_I^{\alpha}\right]\left[r_J^{\gamma} - r_I^{\gamma}\right] + \mathcal{O}\left(h^3\right), \qquad (24)$$

$$m\left(\boldsymbol{r}_J\right) = m\left(\boldsymbol{r}_I\right) + m_{,\alpha}\left(\boldsymbol{r}_I\right)\left[r_J^{\alpha} - r_I^{\alpha}\right] + \mathcal{O}\left(h^2\right). \qquad (25)$$

Substituting relations (24)-(25) into the scheme (21), it leads to the following relations:

$$\sum_{\Omega_{\boldsymbol{r}_I,\tilde{h}_I}} V_{\boldsymbol{r}_J}\left[\mathbf{u}\left(\boldsymbol{r}_J\right) - \mathbf{u}\left(\boldsymbol{r}_I\right)\right]\frac{\left(\boldsymbol{r}_J - \boldsymbol{r}_I\right)\cdot\left(m_J + m_I\right)\cdot\overline{\nabla W}\left(\boldsymbol{r}_J - \boldsymbol{r}_I, \tilde{h}_{IJ}\right)}{\left\|\boldsymbol{r}_J - \boldsymbol{r}_I\right\|^2} =$$

$$= 2m\left(\boldsymbol{r}_I\right)\mathbf{u}_{,\alpha}\left(\boldsymbol{r}_I\right)\sum_{\Omega_{\boldsymbol{r}_I,\tilde{h}_I}} V_{\boldsymbol{r}_J}\overline{\nabla_{\alpha}W}\left(\boldsymbol{r}_J - \boldsymbol{r}_I, \tilde{h}_{IJ}\right) +$$

$$+ m\left(\boldsymbol{r}_I\right)\mathbf{u}_{,\alpha\gamma}\left(\boldsymbol{r}_I\right)\sum_{\Omega_{\boldsymbol{r}_I,h}} V_{\boldsymbol{r}_J}\left[r_J^{\alpha} - r_I^{\alpha}\right]\overline{\nabla_{\gamma}W}\left(\boldsymbol{r}_J - \boldsymbol{r}_I, \tilde{h}_{IJ}\right) + \qquad (26)$$

$$+ m_{,\alpha}\left(\boldsymbol{r}_I\right)\mathbf{u}_{,\gamma}\left(\boldsymbol{r}_I\right)\sum_{\Omega_{\boldsymbol{r}_I,h}} V_{\boldsymbol{r}_J}\left[r_J^{\alpha} - r_I^{\alpha}\right]\overline{\nabla_{\gamma}W}\left(\boldsymbol{r}_J - \boldsymbol{r}_I, \tilde{h}_{IJ}\right) + \mathcal{O}\left(h^2\right).$$

Here, the following relation has been used

$$\left[r_J^{\alpha} - r_I^{\alpha}\right]\frac{\left(r_J^{\gamma} - r_I^{\gamma}\right)\overline{\nabla_{\gamma}W}\left(\boldsymbol{r}_J - \boldsymbol{r}_I, \tilde{h}_{IJ}\right)}{\left\|\boldsymbol{r}_J - \boldsymbol{r}_I\right\|^2} = \overline{\nabla_{\alpha}W}\left(\boldsymbol{r}_J - \boldsymbol{r}_I, \tilde{h}_{IJ}\right), \quad \forall\alpha. \qquad (27)$$

The maximum accuracy is achieved when

$$(a) \sum_{\Omega_{\boldsymbol{r}_I,\tilde{h}_I}} V_{\boldsymbol{r}_J}\overline{\nabla_{\alpha}W}\left(\boldsymbol{r}_J - \boldsymbol{r}_I, \tilde{h}_{IJ}\right) = 0, \quad \forall\alpha,$$

$$(b) \sum_{\Omega_{\boldsymbol{r}_I,\tilde{h}_I}} V_{\boldsymbol{r}_J}\left[r_J^{\alpha} - r_I^{\alpha}\right]\overline{\nabla_{\gamma}W}\left(\boldsymbol{r}_J - \boldsymbol{r}_I, \tilde{h}_{IJ}\right) = \delta_{\alpha\gamma}, \quad \forall\alpha,\gamma, \qquad (28)$$

which is difficult to fulfill simultaneously for different kernel gradients leading to the overall accuracy $\mathcal{O}\left(h^{\omega}\right)$, $0 \leq \omega < 2$. In the subsection 2.1, several options of computing kernel gradients $\overline{\nabla W}(\boldsymbol{r}_J - \boldsymbol{r}_I, \tilde{h}_{IJ})$ (i.e., $\nabla_{\gamma}W$, $\nabla_{\alpha}\overline{W}$, $\overline{\nabla}_{\alpha}\overline{W}$, and $\widetilde{\nabla}_{\alpha}\overline{W}$) are proposed (12), (13), (14), and (15), respectively. The kernel gradient (13) satisfies conditions (27) and (28)(a) but not the condition (28)(b). At the same time, all corrected options $\overline{\nabla^*W}(\boldsymbol{r}_J - \boldsymbol{r}_I, \tilde{h}_{IJ})$ (i.e., ∇_{γ}^*W, $\nabla_{\alpha}^*\overline{W}$, $\overline{\nabla}_{\alpha}^*\overline{W}$, and $\widetilde{\nabla}_{\alpha}^*\overline{W}$) satisfy the condition (28)(b) but not the conditions (27). One may decide to use $\overline{\nabla^*W}(\boldsymbol{r}_J - \boldsymbol{r}_I, \tilde{h}_{IJ})$ in the discretization scheme (21) which leads to the error with the leading term

$$2m\left(\boldsymbol{r}_I\right)\mathbf{u}_{,\alpha}\left(\boldsymbol{r}_I\right)\sum_{\boldsymbol{r}_J \in \Omega_{\boldsymbol{r}_I,\tilde{h}_I}} V_{\boldsymbol{r}_J}\left[r_J - r_I\right]\frac{\left(\boldsymbol{r}_J - \boldsymbol{r}_I\right)\cdot\overline{\nabla^*W}(\boldsymbol{r}_J - \boldsymbol{r}_I, \tilde{h}_{IJ})}{\left\|\boldsymbol{r}_J - \boldsymbol{r}_I\right\|^2}. \qquad (29)$$

This leads to the incorporation of the correction factor into Brookshaw's approximation. A different correction factor has been introduced and investigated in [2]. However, the discretization scheme

(21) with the $\overline{\nabla^* W}(\boldsymbol{r}_J - \boldsymbol{r}_I, \tilde{h}_{IJ})$ kernel gradient is less accurate near the boundary due to the absence of the skew symmetric property of the gradient and remaining singularity in the error term when $\boldsymbol{r}_J = \boldsymbol{r}_I$ which can be removed in the conventional form (26). Alternatively, as was discussed in [2], the correction multiplier can be introduced in (21) defined as $n \cdot [\mathbf{C}_{\alpha\alpha}]^{-1}$ leading to:

$$\langle \nabla \left(m \left(\boldsymbol{r}_I \right) \nabla \mathbf{u} \left(\boldsymbol{r}_I \right) \right) \rangle^* = n \cdot [\mathbf{C}_{\alpha\alpha}]^{-1} \cdot \langle \nabla \left(m \left(\boldsymbol{r}_I \right) \nabla \mathbf{u} \left(\boldsymbol{r}_I \right) \right) \rangle. \tag{30}$$

Figure 1 shows Laplacian values for the function $\nabla^2(x^2 + y^2)$ using original Brookshaw's approximation (21) with (a) conventional kernel $\nabla_\gamma W$, (b) corrected kernel $\nabla_\gamma^* W$ and corrected Brookshaw's approximation (30) with the conventional kernel $\nabla_\gamma W$.
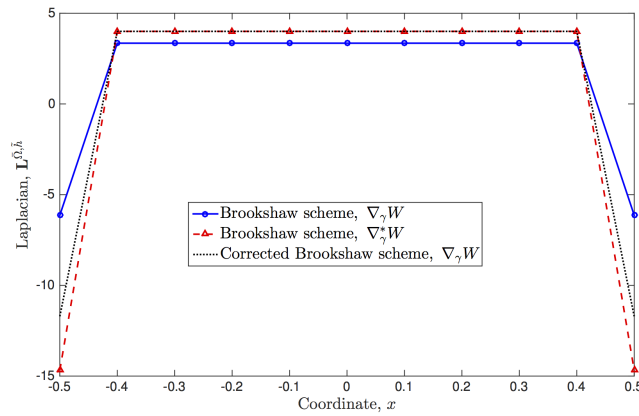

FIGURE 1. Values for $\nabla^2(x^2 + y^2)$ along $y = 0$ using Brookshaw's approximation with (a) conventional kernel $\nabla_\gamma W$, (b) corrected kernel $\nabla_\gamma^* W$ and with the correction multiplier $n \cdot [\mathbf{C}_{\alpha\alpha}]^{-1}$. The numerical domain is a unit square in $\mathbb{R}^2$ with the center at $a_i = 0$, $\forall i$ and side length $L = 1$. The cubic spline (9) was used with $\tilde{h} = f \cdot h_p$, $h_p = 0.1$, $f = 1.0$.

The scheme (21) is widely (almost unconditionally) used in the SPH modeling community. For example, it was used for a thermal conduction [1, 34, 35], for modeling a viscous diffusion [19], for a vortex spin-down [36] and Rayleigh-Taylor instability, for simulating Newtonian and non-Newtonian flows with a free surface [37] for the comparison of weakly compressible and truly incompressible algorithms, for macroscopic and mesoscopic flows [38], for a simulation of a solid-fluid mixture flow [39]. Recently, it has been used to model electrokinetic flows [40], Dam-break problem and Taylor-Green vortex [10].

There are different numerical SPH schemes used in numerical simulations. High order accuracy approximations can also be derived by using the SPH discretization on the higher order Taylor series expansion [2, 24, 25, 41]. However, it is usually required that the discrete numerical schemes can reproduce linear fields [13, 14, 28, 42] or polynomials up to a given order [43, 44].

2.4. **Schwaiger's scheme (2008).** The correction terms to the Brookshaw formulation which improve the accuracy of the Laplacian operator near boundaries were proposed by Schwaiger in [2]:

$$-\frac{n}{\Gamma_{kk}^{-1}} \langle \nabla \left(m\left(\boldsymbol{r}_I\right) \nabla \mathbf{u}\left(\boldsymbol{r}_I\right) \right) \rangle =$$

$$\left\{ \sum_{\Omega_{\boldsymbol{r}_I, \tilde{h}_I}} V_{\boldsymbol{r}_J} \left[\mathbf{u}\left(\boldsymbol{r}_J\right) - \mathbf{u}\left(\boldsymbol{r}_I\right) \right] \frac{\left(\boldsymbol{r}_J - \boldsymbol{r}_I\right) \cdot \left(m_J + m_I\right) \overline{\nabla W}\left(\boldsymbol{r}_J - \boldsymbol{r}_I, \tilde{h}_{IJ}\right)}{\left\| \boldsymbol{r}' - \boldsymbol{r} \right\|^2} \right\} - \tag{31}$$

$$- \left\{ \left[\langle \nabla_\alpha \left(m\left(\boldsymbol{r}_I\right) \mathbf{u}\left(\boldsymbol{r}_I\right) \right) \rangle - \mathbf{u}\left(\boldsymbol{r}_I\right) \langle \nabla_\alpha m\left(\boldsymbol{r}_I\right) \rangle + m\left(\boldsymbol{r}_I\right) \langle \nabla_\alpha \mathbf{u}\left(\boldsymbol{r}_I\right) \rangle \right] \mathbf{N}^\alpha \right\},$$

$$\mathbf{N}^\alpha\left(\boldsymbol{r}_I\right) = \left[\sum_{\Omega_{\boldsymbol{r}_I, \tilde{h}_I}} V_{\boldsymbol{r}_J} \overline{\nabla_\alpha W}\left(\boldsymbol{r}_I - \boldsymbol{r}_J, \tilde{h}_{IJ}\right) \right], \tag{32}$$

$$\langle \nabla_\alpha \mathbf{u}\left(\boldsymbol{r}_I\right) \rangle = \sum_{\Omega_{\boldsymbol{r}_I, \tilde{h}_I}} V_{\boldsymbol{r}_J} \left[\mathbf{u}\left(\boldsymbol{r}_J\right) - \mathbf{u}\left(\boldsymbol{r}_I\right) \right] \overline{\nabla_\alpha^* W}\left(\boldsymbol{r}_I - \boldsymbol{r}_J, \tilde{h}_{IJ}\right), \tag{33}$$

where $n = 1, 2, 3$ is the spatial dimension and the tensor $\Gamma_{\alpha\beta}$ is defined by

$$\Gamma_{\alpha\beta}\left(\boldsymbol{r}_I\right) = \sum_{\Omega_{\boldsymbol{r}_I, \tilde{h}_I}} V_{\boldsymbol{r}_J} \frac{\left(r_J^\gamma - r_I^\gamma\right) \overline{\nabla_\gamma W}\left(\boldsymbol{r}_J - \boldsymbol{r}_I, \tilde{h}_{IJ}\right)}{\left\| \boldsymbol{r}' - \boldsymbol{r} \right\|^2} \left(r_J^\alpha - r_I^\alpha\right) \left(r_J^\beta - r_I^\beta\right). \tag{34}$$

The gradient $\langle \nabla_\alpha \mathbf{u}\left(\boldsymbol{r}_I\right) \rangle$ is the corrected gradient which can reproduce linear fields [28, 42]. For multi-dimensional problems, the correction tensor $\Gamma_{\alpha\beta}\left(\mathbf{r}_I\right)$ is a matrix. If the particle $\mathbf{r}_I$ has entire stencil support (i.e., the domain support for all kernels $W\left(\mathbf{r}_J - \mathbf{r}_I, \tilde{h}_{IJ}\right)$ is entire and symmetric) then $\Gamma_{\alpha\beta}\left(\mathbf{r}_I\right) \approx \delta_{\alpha\beta}$.

Remark 1. *It is important to note that correction tensors* $\Gamma_{\alpha\beta}$ *and* $\mathbf{C}_{\alpha\beta}^{-1}$ *are the same tensors. Indeed, using the following identity:*

$$\left[\mathbf{r}_J^\alpha - \mathbf{r}_I^\alpha\right] \frac{\left(r_J^\gamma - r_I^\gamma\right) \overline{\nabla_\gamma W}\left(\boldsymbol{r}_J - \boldsymbol{r}_I, \tilde{h}_{IJ}\right)}{\left\| \boldsymbol{r}_J - \boldsymbol{r}_I \right\|^2} =$$

$$= \frac{1}{h} \frac{\overline{dW}}{dz} \frac{\left[r_J^\alpha - r_I^\alpha\right]}{\left\| \boldsymbol{r}_J - \boldsymbol{r}_I \right\|} = \overline{\nabla_\alpha W}\left(\boldsymbol{r}_J - \boldsymbol{r}_I, \tilde{h}_{IJ}\right), \quad \forall \alpha; \quad \frac{\overline{dW}}{dz} \leq 0, \tag{35}$$

where $\dfrac{\overline{dW}}{dz}$ *is computed using either conventional* W *or normalized* $\overline{W}$ *kernels,* $z = \left\| \boldsymbol{r}_J - \boldsymbol{r}_I \right\| / \tilde{h}$, $\forall \boldsymbol{r}_J, \boldsymbol{r}_I \in \Omega \subset \mathbb{R}^n$, *the following relation can be established:*

$$\Gamma_{\alpha\beta}\left(\boldsymbol{r}_I\right) = \sum_{\Omega_{\boldsymbol{r}_I, \tilde{h}_I}} V_{\boldsymbol{r}_J} \frac{\left(r_J^\gamma - r_I^\gamma\right) \overline{\nabla_\gamma W}\left(\boldsymbol{r}_J - \boldsymbol{r}_I, \tilde{h}_{IJ}\right)}{\left\| \boldsymbol{r}_J - \boldsymbol{r}_I \right\|^2} \left(r_J^\alpha - r_I^\alpha\right) \left(r_J^\beta - r_I^\beta\right) =$$

$$= \sum_{\Omega_{\boldsymbol{r}_I, \tilde{h}_I}} V_{\boldsymbol{r}_J} \left[r_J^\alpha - r_I^\alpha\right] \overline{\nabla_\beta W}\left(\boldsymbol{r}_J - \boldsymbol{r}_I, \tilde{h}_{IJ}\right) = \mathbf{C}_{\alpha\beta}^{-1}\left(\boldsymbol{r}_I\right). \tag{36}$$

In addition, it is important to note that

$$\Gamma_{\alpha\alpha} = \sum_{\Omega_{\boldsymbol{r}_I, \tilde{h}_I}} V_{\boldsymbol{r}_J} \left(\boldsymbol{r}_J^\gamma - \boldsymbol{r}_I^\gamma \right) \cdot \overline{\nabla_\gamma^* W} \left(\boldsymbol{r}_J - \boldsymbol{r}_I, \tilde{h}_{IJ} \right) = n \tag{37}$$

in the case of using the corrected gradient and, hence, $\dfrac{\Gamma_{kk}^{-1}}{n} = 1$. However, $\overline{\nabla_\gamma^* W}$ does not satisfy relation (35).

For multi-dimensional problems, the correction tensor $\Gamma_{\alpha\beta}\left(\boldsymbol{r}_I\right)$ is a matrix. If the particle $\boldsymbol{r}_I$ has entire stencil support (i.e., the domain support for all kernels $W\left(\boldsymbol{r}_J - \boldsymbol{r}_I, \tilde{h}_{IJ}\right)$ is entire and symmetric) then $\Gamma_{\alpha\beta}\left(\boldsymbol{r}_I\right) \approx \delta_{\alpha\beta}$. Unfortunately, $\Gamma_{\alpha\beta}\left(\boldsymbol{r}_I\right)$ deviates from $\delta_{\alpha\beta}$ for the provided algorithm and, hence, it is important to minimize this deviation from $\delta_{\alpha\beta}$ in the new methods.

To calculate coefficients in the scheme (31)–(34) is a trivial task. However, in general, it should be performed at each Newton-Raphson iteration in the non-linear case (i.e., $m = m\left(\mathbf{u}\left(\boldsymbol{r}_I\right)\right)$). It also requires additional efforts to invert the correction matrix $\mathbf{A}_{\alpha\beta}$ (inversion of $n \times n$ matrices per each particle, where $n = 1, 2, 3$ is the spatial dimension) and storage cost of $\overline{\nabla_\alpha W}\left(\mathbf{r}_J - \mathbf{r}_I, h\right)$, $\overline{\nabla_\alpha^* W}\left(\mathbf{r}_J - \mathbf{r}_I, h\right)$, and corresponding $\Gamma_{\alpha\alpha}^{-1} = \mathbf{A}_{\alpha\alpha}^{-1}$ per each particle.

Furthermore, additional terms proposed by Schwaiger [2] reduce to

$$\left[\langle m\left(\boldsymbol{r}_I\right)\mathbf{u}\left(\boldsymbol{r}_I\right)\rangle - \mathbf{u}\left(\boldsymbol{r}_I\right)\langle m\left(\boldsymbol{r}_I\right)\rangle + m\left(\boldsymbol{r}_I\right)\langle\mathbf{u}\left(\boldsymbol{r}_I\right)\rangle\right]\mathbf{N} =$$
$$= 2m\left(\boldsymbol{r}_I\right)\nabla\mathbf{u}\left(\boldsymbol{r}_I\right) \cdot \mathbf{N} + \mathcal{O}\left(\tilde{h}_I^2\right) \tag{38}$$

which is the leading term outlined in (26). However, if one uses $\overline{\nabla^* W}(\boldsymbol{r}_J - \boldsymbol{r}_I, \tilde{h}_{IJ})$ in the first term of the discretization scheme (31) then the definition for $\mathbf{N}^\alpha$ has to be modified in accordance of (29) to maintain the higher order discretization accuracy, for example, as:

$$\widetilde{\mathbf{N}}^\alpha = \sum_{\Omega_{\boldsymbol{r}_I, \tilde{h}_I}} V_{\boldsymbol{r}_J} \left[\boldsymbol{r}_J^\alpha - \boldsymbol{r}_I^\alpha\right] \frac{\left(\boldsymbol{r}_J - \boldsymbol{r}_I\right)\overline{\nabla^* W}\left(\boldsymbol{r}_J - \boldsymbol{r}_I, \tilde{h}_{IJ}\right)}{\left\|\boldsymbol{r}_J - \boldsymbol{r}_I\right\|^2}, \quad \forall\alpha \tag{39}$$

which reduces to the conventional $\mathbf{N}^\alpha$ in the case of $\overline{\nabla W}(\boldsymbol{r}_J - \boldsymbol{r}_I, \tilde{h}_{IJ})$ due to (35). Figure 2 shows the Laplacian for the function $\nabla^2(x^2 + y^2)$ using Schwaiger's approximation (31)–(34) with (a) conventional kernel $\nabla_\gamma W$ and (b) corrected kernel $\nabla_\gamma^* W$.

Finally, the discretization scheme (31)–(34) is at least $\mathcal{O}\left(h^\omega\right)$, $1 \leq \omega \leq 2$ order of accuracy in average for any scalar mobility field $m\left(\boldsymbol{r}\right) \in C^1\left(\Omega\right)$, $m\left(\boldsymbol{r}\right) \geq 0$ everywhere within the numerical domain $\Omega \in \mathbb{R}^n$ sufficiently far away from the boundary $\partial\Omega$.

3. Meshless Transmissibilities

The well-known two-point flux approximation (TPFA) is a mesh dependent numerical scheme used in solving elliptic equation (1): $\mathbf{L}\left(\mathbf{u}\right) = 0$ with the diagonal matrix of coefficients $\mathbf{M}$. The net flow rate from a cell I into neighboring cells in this scheme is obtained by summing fluxes over the neighboring cells J:

$$\boldsymbol{q} = \sum_J \widetilde{T}_{JI}\left[\mathbf{u}\left(\boldsymbol{r}_J\right) - \mathbf{u}\left(\boldsymbol{r}_I\right)\right], \ \widetilde{T}_{JI} \geq 0, \tag{40}$$

where $\widetilde{T}_{JI}$ is the transmissibility between cells J and I, $\boldsymbol{q}$ is the total flux through the boundary of the control volume located at the point $\boldsymbol{r}_I$. The transmissibility $\widetilde{T}_{JI}$ defined at an interior face
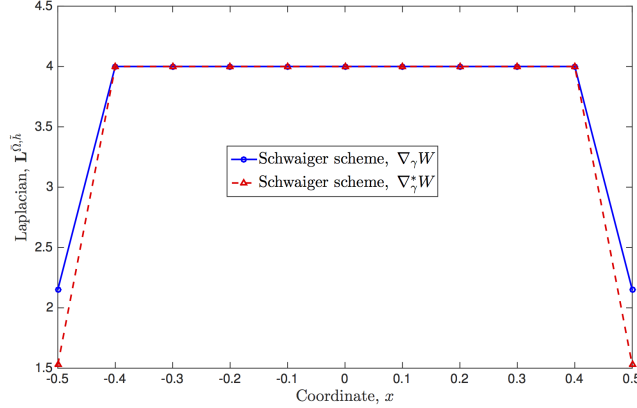
FIGURE 2. Values for $\nabla^2(x^2 + y^2)$ along $y = 0$ using Schwaiger's approximation with (a) conventional kernel $\nabla_\gamma W$ and (b) corrected kernel $\nabla_\gamma^* W$. The numerical domain is a unit square in in $\mathbb{R}^2$ with the center at $a_i = 0$, $\forall i$. The cubic spline (9) was used with $\tilde{h} = f \cdot h_p$, $h_p = 0.1$, $f = 1.0$.

f between cells J and I is calculated as

$$\widetilde{T}_{JI} = \frac{1}{\left[\dfrac{\|\boldsymbol{r}_{f,J}\|^2}{\boldsymbol{S}_f \mathbf{M} \boldsymbol{r}_{f,J}} + \dfrac{\|\boldsymbol{r}_{f,I}\|^2}{\boldsymbol{S}_f \mathbf{M} \boldsymbol{r}_{f,I}} \right]}, \tag{41}$$

where $\boldsymbol{r}_{f,J}$ and $\boldsymbol{r}_{f,I}$ are the vectors from centers of cells J and I to the face f respectively, $\boldsymbol{S}_f$ is the area vector of the face f. In the case of $\mathbf{M}$-orthogonal mesh, when $\mathbf{M}\boldsymbol{S}_f$ and $[\boldsymbol{r}_J - \boldsymbol{r}_I]$ are collinear, the expression (40) reduces to the form of the central finite difference scheme and approximates the flux with $\mathcal{O}\left(h^2\right)$ order of accuracy for any mobility tensor field $\mathbf{M}$. The expression (41) ensures that the flux into the adjoining region is continuous [34]. The TPFA scheme (40) is the unconditionally monotone scheme.

It is clear that the expression (31) cannot be written in the form (40) due to terms $\langle \nabla_\alpha \left(m \left(\boldsymbol{r}_I \right) \mathbf{u} \left(\boldsymbol{r}_I \right) \right) \rangle \mathbf{N}^\alpha$ and $\mathbf{u} \left(\boldsymbol{r}_I \right) \langle \nabla_\alpha m \left(\boldsymbol{r}_I \right) \rangle \mathbf{N}^\alpha$. Hence, it is only possible in this case to introduce a definition of a partial meshless transmissibility between particles $\boldsymbol{r}_J$ and $\boldsymbol{r}_I$ as follows:

$$T^P \left(\boldsymbol{r}_J, \boldsymbol{r}_I \right) = T_{JI}^P = \frac{\Gamma_{\beta\beta}^{-1}}{n} \times V_{\boldsymbol{r}_J}$$

$$\left\{ \frac{\left(\boldsymbol{r}_J - \boldsymbol{r}_I \right) \cdot \left(m_J + m_I \right) \cdot \overline{\nabla W} \left(\boldsymbol{r}_J - \boldsymbol{r}_I, \tilde{h}_{IJ} \right)}{\|\boldsymbol{r}_J - \boldsymbol{r}_I\|^2} - m_I \overline{\nabla W} \left(\boldsymbol{r}_J - \boldsymbol{r}_I, \tilde{h}_{IJ} \right) \mathbf{N}^\alpha \right\}. \tag{42}$$

It is important to note that transmissibilities T_{JI}^P and $\widetilde{T}_{JI}^P$ have different physical units. Furthermore, it raises the question wherever the scheme (31)–(34) is monotone.

Using Taylor series expansions about a point $\boldsymbol{r}_I$, i.e. relations (24), (25), the expression (38) can be written keeing higher order error terms as:

$$[\langle \nabla_\alpha \left(m\left(\boldsymbol{r}_I\right) \mathbf{u}\left(\boldsymbol{r}_I\right)\right)\rangle - \mathbf{u}\left(\boldsymbol{r}_I\right) \langle \nabla_\alpha m\left(\boldsymbol{r}_I\right)\rangle + m\left(\boldsymbol{r}_I\right) \langle \nabla_\alpha \mathbf{u}\left(\boldsymbol{r}_I\right)\rangle] =$$

$$2m\left(\boldsymbol{r}_I\right) \left(\mathbf{u}_{,\alpha}\left(\boldsymbol{r}_I\right) + \frac{1}{2}\mathbf{u}_{,\omega\gamma}\left(\boldsymbol{r}_I\right) \sum_{\Omega_{\boldsymbol{r}_I,\tilde{h}_I}} V_{\boldsymbol{r}_J} \left[r_J^\omega - r_I^\omega\right]\left[r_J^\gamma - r_I^\gamma\right]\overline{\nabla_\alpha^* W}\left(\boldsymbol{r}_J - \boldsymbol{r}_I, \tilde{h}_{IJ}\right) \right) + \tag{43}$$

$$+\mathcal{O}\left(\tilde{h}_I^3\right).$$

Hence, there is an additional term that has not been taken into account in (31)–(34). The following section describes an alternative numerical scheme for the heterogeneous Laplace operator. Some initial attemps were also made in [45].

3.1. **New scheme.** The correction terms to the Brookshaw [1] and Schwaiger [2] formulations which improve the accuracy of the Laplacian operator near boundaries can be done as follows:

$$-\frac{n}{\bar{\Gamma}_{\beta\beta}^{-1}} \langle \nabla \left(\mathbf{M}\left(\boldsymbol{r}_I\right) \nabla \mathbf{u}\left(\boldsymbol{r}_I\right)\right)\rangle =$$

$$\left\{ \sum_{\Omega_{\boldsymbol{r}_I,\tilde{h}_I}} V_{\boldsymbol{r}_J} \left[\mathbf{u}\left(\boldsymbol{r}_J\right) - \mathbf{u}\left(\boldsymbol{r}_I\right)\right] \frac{\left(\boldsymbol{r}_J - \boldsymbol{r}_I\right) \cdot \left(\mathbf{M}_J + \mathbf{M}_I\right) \cdot \overline{\nabla W}\left(\boldsymbol{r}_J - \boldsymbol{r}_I, \tilde{h}_{IJ}\right)}{\|\boldsymbol{r}_J - \boldsymbol{r}_I\|^2} \right\} - $$

$$-\left\{ \mathbf{N} \cdot \left(\sum_{\Omega_{\boldsymbol{r}_I,\tilde{h}_I}} V_{\boldsymbol{r}_J} \cdot \left(\mathbf{M}_J + \mathbf{M}_I\right) \cdot \left[\mathbf{u}\left(\boldsymbol{r}_J\right) - \mathbf{u}\left(\boldsymbol{r}_I\right)\right] \overline{\nabla^* W}\left(\boldsymbol{r}_J - \boldsymbol{r}_I, \tilde{h}_{IJ}\right)\right)\right\}, \tag{44}$$

where $n = 1, 2, 3$ is the spatial dimension and tensor $\bar{\Gamma}_{\alpha\beta}$ is defined by

$$\bar{\Gamma}_{\alpha\beta}\left(\boldsymbol{r}_I\right) = \begin{cases} \Gamma_{\alpha\beta}^*\left(\boldsymbol{r}_I\right), & \Gamma_{\alpha\beta}^*\left(\boldsymbol{r}_I\right) \neq 0, \\ \Gamma_{\alpha\beta}\left(\boldsymbol{r}_I\right), & \Gamma_{\alpha\beta}^*\left(\boldsymbol{r}_I\right) = 0 \end{cases} \tag{45}$$

where

$$\Gamma_{\alpha\beta}^*\left(\boldsymbol{r}_I\right) = \sum_{\Omega_{\boldsymbol{r}_I,\tilde{h}_I}} V_{\boldsymbol{r}_J} \left[r_J^\beta - r_I^\beta\right] \overline{\nabla_\alpha W}\left(\boldsymbol{r}_J - \boldsymbol{r}_I, \tilde{h}_{IJ}\right) -$$

$$-\mathbf{N}^\gamma \sum_{\Omega_{\boldsymbol{r}_I,\tilde{h}_I}} V_{\boldsymbol{r}_J} \left[r_J^\alpha - r_I^\alpha\right]\left[r_J^\beta - r_I^\beta\right] \overline{\nabla_\gamma^* W}\left(\boldsymbol{r}_J - \boldsymbol{r}_I, \tilde{h}_{IJ}\right). \tag{46}$$

Following (44), we only need to compute the trace of the matrix $\Gamma_{\alpha\beta}^*\left(\boldsymbol{r}_I\right)$. Furthermore, it is important to note the following remark.

Remark 2. *The following relations can be written:*

$$\Gamma_{\beta\beta}^*\left(\boldsymbol{r}_I\right) = \sum_{\Omega_{\boldsymbol{r}_I,\tilde{h}_I}} V_{\boldsymbol{r}_J} \|\boldsymbol{r}_J - \boldsymbol{r}_I\| \frac{1}{\tilde{h}_{IJ}} \frac{\overline{dW}}{dz} -$$

$$-\mathbf{N}^\gamma \sum_{\Omega_{\boldsymbol{r}_I,\tilde{h}_I}} V_{\boldsymbol{r}_J} \|\boldsymbol{r}_J - \boldsymbol{r}_I\|^2 \overline{\nabla_\gamma^* W}\left(\boldsymbol{r}_J - \boldsymbol{r}_I, \tilde{h}_{IJ}\right), \quad \frac{\overline{dW}}{dz} \leq 0. \tag{47}$$

$$\left| \overline{\nabla_\alpha^* W} \mathbf{N}^\alpha \left(\boldsymbol{r}_I \right) \right| \leq \max_{z \in \Upsilon} \left(\overline{\frac{dW}{dz}} \right)^2 \cdot \tilde{h} \cdot \| C_{\alpha\beta} \| \cdot V_\Omega \cdot \left\| \frac{\sum\limits_{\boldsymbol{r}_\xi \in \Omega_{\boldsymbol{r}_I, \tilde{h}_I}} V_\xi \cdot \boldsymbol{r}_\xi}{V_{\Omega_{\boldsymbol{r}_I, \tilde{h}_I}}} - \boldsymbol{r}_I \right\|, \qquad (48)$$

where $z = \| \boldsymbol{r}_J - \boldsymbol{r}_I \| / \tilde{h}_{IJ}$, $\Upsilon = supp\ \overline{\frac{dW}{dz}}$, $\| C_{\alpha\beta} \|$ is the matrix norm of $C_{\alpha\beta}$, $V_{\Omega_{\boldsymbol{r}_I, \tilde{h}_I}}$ is the volume of $\Omega_{\boldsymbol{r}_I, \tilde{h}_I}$. It follows that if $\left\| \frac{\sum V_\xi \boldsymbol{r}_\xi}{V_{\Omega_{\boldsymbol{r}_I, \tilde{h}_I}}} - \boldsymbol{r}_I \right\| \leq \tilde{h}_I$ then there is a parameter $\tilde{h}_I$ such that $\Gamma_{\beta\beta}^* \left(\boldsymbol{r}_I \right) \leq 0$.

The reason for having the correction factor in the form (45)–(46) is that $\Gamma_{\alpha\beta}^* \left(\boldsymbol{r}_I \right) = 0$ in some cases, where particles have the incomplete Kernel support (e.g., at the corners and boundaries of the numerical domain). For multi-dimensional problems, the correction tensor $\bar{\Gamma}_{\alpha\beta} \left(\boldsymbol{r}_I \right)$ is also a matrix. If the particle $\boldsymbol{r}_I$ has entire stencil support (i.e., the domain support for all kernels $W \left(\boldsymbol{r}_J - \boldsymbol{r}_I, \tilde{h}_{IJ} \right)$ is completed and symmetric) then $\bar{\Gamma}_{\alpha\beta} \left(\boldsymbol{r}_I \right) \approx \delta_{\alpha\beta}$. The proposed correction matrix deviates less from the unit matrix compare to (34). As a result, the discretization scheme (44)–(46) is at least $\mathcal{O} \left(h^\omega \right)$, $1 \leq \omega \leq 2$ order of accuracy in average for any scalar mobility field $m \left(\boldsymbol{r} \right) \geq 0, m \left(\boldsymbol{r} \right) \in C^1 \left(\Omega \right)$, $\mathbf{M}^{\alpha\beta} \left(\boldsymbol{r} \right) = m \left(\boldsymbol{r} \right) \delta_{\alpha\beta}$ everywhere within the numerical domain $\Omega \in \mathbb{R}^n$ sufficiently far away from the boundary $\partial\Omega$. The scheme has the two-point flux approximation nature and can be written in the form of (2), which can be proved using the arguments above. The scheme (44)–(46) is in line with an alternative formulation for continuum mechanics called the peridynamic model [46, 47], which was proposed several years ago.

All presented schemes in this paper do not require exact expressions for the gradient (i.e., spatial derivatives) of the mobility field $\nabla_\gamma m \left(\boldsymbol{r} \right)$ to keep a higher order of accuracy for any mobility field. Hence, this scheme can be used with the discontinuous (or piecewise continuous) mobility field $m \left(\boldsymbol{r} \right) \in L_2 \left(\Omega \right)$. It is important to note that Brookshaw [1] and Schwaiger [2] schemes can also be written for the diagonal mobility matrix $\mathbf{M}^{\alpha\beta} \left(\boldsymbol{r} \right)$ by substituting $\mathbf{M}^{\alpha\beta}$ into (21) and (31) instead of $m \left(\boldsymbol{r} \right)$ and performing summation by repeating indices.

4. Approximation, Stability, and Monotonicity

The approximation, stability and monotonicity are important properties of numerical schemes which provide and quantify the confidence in the numerical modeling and results from corresponding simulations. Therefore, in order to be confident that the proposed numerical schemes provide the adequate accuracy of the elliptic operator (1), several numerical analyses to identify the order of approximation, stability and monotonicity have been performed. It is important to recall that all numerical schemes are characterized by two length scales: $\tilde{h} = f \cdot h_p$ is the radius of $\Omega_{\boldsymbol{r}, \tilde{h}} = \text{supp} W$, and h_p is the inter-particle distance. Hence, while investigating the approximation of the meshless discretization scheme, it is important to distinguish two cases: (a) the neighborhood number of particles is fixed $f = \text{const}$ with varying the inter-particle distance, (b) the inter-particle distance is fixed $h_p = \text{const}$ with varying the neighborhood number of particles. The first case will be analyzed by looking at the error defined by

$$\| E \|_\Omega^{L_2} = \left[\frac{1}{\sum\limits_J V_{\boldsymbol{r}_J}} \sum_J V_{\boldsymbol{r}_J} \left(\mathbf{L} \left[\mathbf{u} \left(\boldsymbol{r}_J \right) \right] - \langle \mathbf{L} \rangle \left[\mathbf{u} \left(\boldsymbol{r}_J \right) \right] \right)^2 \right]^{1/2}, \qquad (49)$$

where $\mathbf{L}[\cdot]$ is the analytical Laplacian at the particle $\boldsymbol{r}_J$ and $\langle\mathbf{L}\rangle[\cdot]$ is the approximation of the Laplacian at the particle $\boldsymbol{r}_J$, $\|E\|_{\Omega}^{L^2}$ is the averaged error over the entire domain. In the following paragraph, the numerical analysis is performed for various functions, particle distributions, and media properties.

Following the work [2], the ability of the discretization to reproduce the Laplacian was tested for several functions in $\mathbb{R}^n$, $n = 1, 2, 3$:

$$(a)\ \boldsymbol{u}^s(\boldsymbol{x}) = \sum_{i=1}^{n} x_i^s, \quad (b)\ \boldsymbol{u}_m^s(\boldsymbol{x}) = \prod_{i=1}^{n} x_i^{m_i}, \ |m| = s \qquad (50)$$

where $m = (m_1, \ldots, m_n)$, $\forall i : m_i \geq 0$ is the n-dimensional multi-index with the property $|m| = \sum_{i=1}^{n} m_i$. The reason for selecting these testing polynomials is as follows. Since the functional space $L_p(\Omega)$ is separable, the above polynomials form the everywhere dense subset of the $L_p(\Omega)$. Hence, any function $\mathbf{u} \in L_p$ can be approximated in L_p using linear combination of the above polynomials leading to the following relations:

$$\mathbf{u}(\boldsymbol{r}) \approx \sum_{k=1}^{\infty} \sum_{|m| \leq k} a_m \left(\prod_{i=1}^{n} x_i^{m_i} \right), \mathbf{M}(\boldsymbol{r}) \approx \sum_{k=1}^{\infty} \sum_{|m| \leq k} b_m \left(\prod_{i=1}^{n} x_i^{m_i} \right). \qquad (51)$$

The approximation error produced by the discretization schemes and considered in this paper for the polynomials $\boldsymbol{u}^s(\boldsymbol{x})$ and $\boldsymbol{u}_m^s(\boldsymbol{x})$ gives the information about the error growth for the arbitrary function $\mathbf{u}(\boldsymbol{r})$. In each test, the homogenous and heterogeneous particle distribution varying the smoothing length $\tilde{h}$ and inter-particle distance h_p are used to study the approximation properties of the proposed discretization scheme.

4.1. **Isotropic Homogeneous Media.** Note that in the limit of the homogeneous isotropic media (i.e., $\mathbf{M}^{\alpha\beta}(\boldsymbol{r}) = m(\boldsymbol{r})\delta_{\alpha\beta}$, $m(\boldsymbol{r}) = 1$) and without the source term, the aforementioned operator $\mathbf{L}(\mathbf{u})$ in (1) reduces to the conventional Laplacian operator (i.e., $\mathbf{L}(\mathbf{u}) \equiv \nabla^2\mathbf{u}$). The domain for the patch test is a unit square similar to [2] for $n = 2$:

$$\Omega = \left\{ \boldsymbol{r} = \{x_i\} \in \mathbb{R}^n \mid \ |x_i - 2.5| \leqslant \frac{1}{2} \ \forall i \right\}$$

with $N = 21$ particles in each direction characterized by two length spacings: $\tilde{h} = f \cdot h_p$, $h_p = 0.05$, $f = 1.2$.

In all of the following tests, the results are displayed along the cross-section $y = 2.5$ in $\mathbb{R}^n$, $n = 2$ (similar to [2] for $n = 2$). In each test, the following discretizations are compared: corrected Brookshaw's scheme (CB-SPH) (30), Schwaiger's scheme (S-SPH) (31)–(34), and new proposed scheme (M-SPH) (44)–(46). Note that the Schwaiger's scheme was tested against several schemes published in [30], [23] and show better accuracy; hence, schemes in [30], [23] are not considered in this paper. The comparison of different schemes starts with test functions of the form $\mathbf{u}^s(\boldsymbol{x})$ described by (50)(a) in $\mathbb{R}^n$, $n = 2$. Plots of the Laplacian approximations and the relative errors defined by (49) for the case $m = 3$ are shown in Figure 3.

The new scheme (M-SPH) has the greatest accuracy at the boundary and is accurate to machine precision ε in the interior. The error plot is shown in Figure 4 along with test functions with exponents from $m = 4, ..., 7$. For these functions, the proposed scheme (44)–(46) is uniformly more accurate for the various experiments. The same behavior is observed in 3D where the M-SPH scheme with the $\nabla_\alpha \overline{W}$ is the most accurate scheme. Furthermore, the new scheme should be
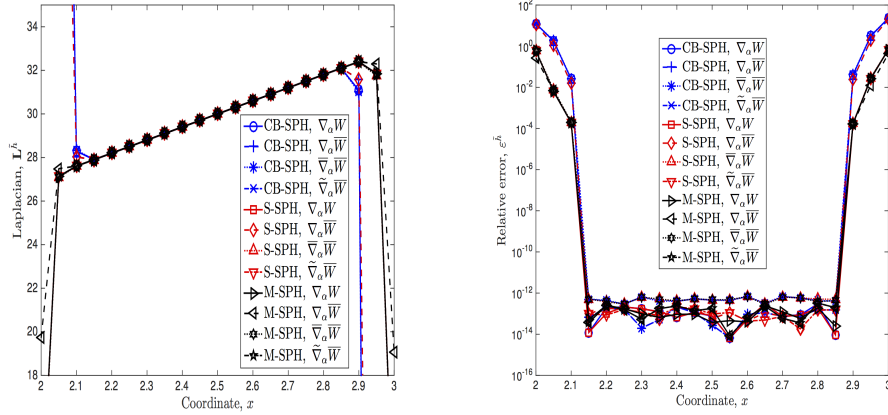
FIGURE 3. Cross-section of the test patch at $y = 2.5$. Three SPH approximations of $\nabla^2 \left(x^3 + y^3\right)$ with different kernel gradients are shown. Corrected Brookshaw's scheme (CB-SPH) is given by (30) with the correction multiplier, while Schwaiger's scheme (S-SPH) is given by (31)–(34). New approximation (M-SPH) considered here is the SPH form (44)–(46). In this case, the Schwaiger's scheme and new scheme have comparable accuracy at the boundaries and are accurate in the interior to the machine precision. Four different options of computing the kernel gradient (i.e., $\nabla_\gamma W$, $\nabla_\alpha \overline{W}$, and corrected kernel gradients (i.e., $\nabla_\alpha^* W$, $\nabla_\alpha^* \overline{W}$, $\overline{\nabla}_\alpha^* \overline{W}$, and $\widetilde{\nabla}_\alpha^* \overline{W}$) are shown.

tested for the functions requiring cross-derivatives as was reported in [2]. To examine the effect of the cross-derivative terms, the same suite of tests was run with the function $\boldsymbol{u}_m^s\left(\boldsymbol{x}\right)$ described by (50)(b) in $\mathbb{R}^n$, $n = 2, 3$. Relative errors for $(xy)^m$ on a same array as in Figure 3 along $y = 2.5$ were computed and again the proposed scheme (44)–(46) was uniformly more accurate for the various experiments. The behavior of each discretization is similar to that shown in Figure 3. The proposed new scheme (M-SPH) performed nearly as well as the Schwaiger's scheme at the boundary. The CB-SPH and S-SPH forms also perform with greater accuracy than all other forms in the interior except in the case with the highest exponent.

An additional concern is that although it deviates from the exact solution near boundaries, it acquires no off-diagonal terms due to the alignment of the array of particles and the boundaries with the coordinate axes. To test the accuracy of the new approximations when there are off-diagonal terms, an array with particles rotated 45° was used with the test function $(xy)^m$ (similar to [2]). The new proposed scheme formulation performs consistently well for lower exponents.

4.2. **Isotropic Heterogeneous Media.** In isotropic heterogeneous media, i.e., $\mathbf{M}^{\alpha\beta}\left(\boldsymbol{r}\right) = m\left(\boldsymbol{r}\right)\delta_{\alpha\beta}$, the Laplace operator takes the general form written in (1). The numerical domain is the same as in the previous section with the same number of particles and particle length scales: $\tilde{h} = f \cdot h_p$, $h_p = 0.05$, $f = 1.2$. Plots of the Laplacian approximations and the relative errors defined by (49) for the case of heterogeneous mobility with $m = 1$ (see (51)) are shown in Figure 5. The new scheme (M-SPH) has the best accuracy at the boundary and is accurate to machine precision ε in the interior. The error plot is shown in Figure 6 along with test functions with exponents from
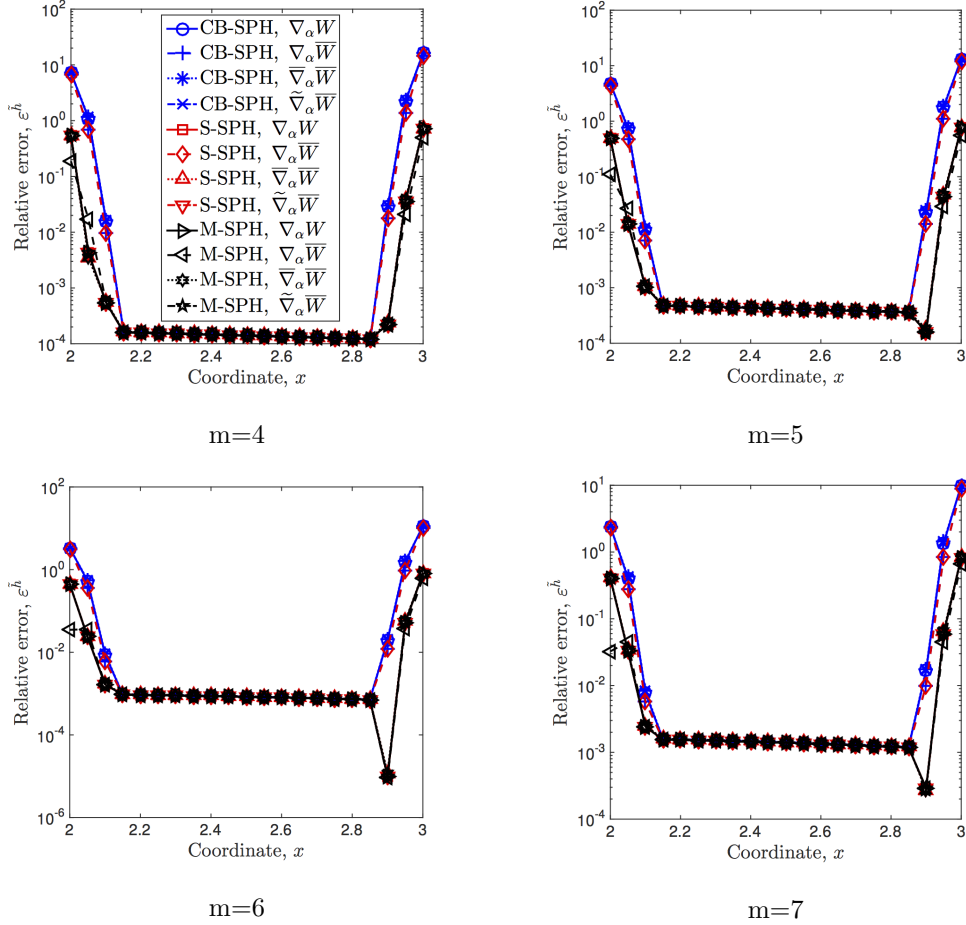
FIGURE 4. The relative errors along $y = 2.5$ for each of the discretizations used in Figure 3 are shown here for the suite of functions $\nabla^2 (x^m + y^m)$ where $m = 4, \ldots, 7$. Four different options of computing the kernel gradients (i.e., $\nabla_\gamma W$, $\nabla_\alpha \overline{W}$, and corrected kernel gradients (i.e., $\nabla_\gamma^* W$, $\nabla_\alpha^* \overline{W}$, $\overline{\nabla}_\alpha^* \overline{W}$, and $\widetilde{\nabla}_\alpha^* \overline{W}$) are shown.

$m = 2, ..., 5$. For these functions, the proposed scheme (44)-(46) is uniformly more accurate for the different increasing exponents. The same behavior is observed in 3D where M-SPH scheme with the $\nabla_\alpha \overline{W}$ is the most accurate scheme.

4.3. **von Neumann stability analysis.** For linear PDEs, there is the Lax-equivalence theorem which connects the consistency and stability with the convergence. The idea of the von Neumann stability analysis is to study the growth of waves $\lambda e^{i\boldsymbol{k} \cdot \boldsymbol{r}}$ (similar to Fourier methods). After applying one of the discretization methods above to the Laplace operator (1), the following relation can be written:

$$\frac{\{\mathbf{u}\}^{n+1} - \{\mathbf{u}\}^n}{\tau} - \mathbf{L}^{\tilde{h}} [\{\mathbf{u}\}^n] = \{\boldsymbol{b}\}, \tag{52}$$
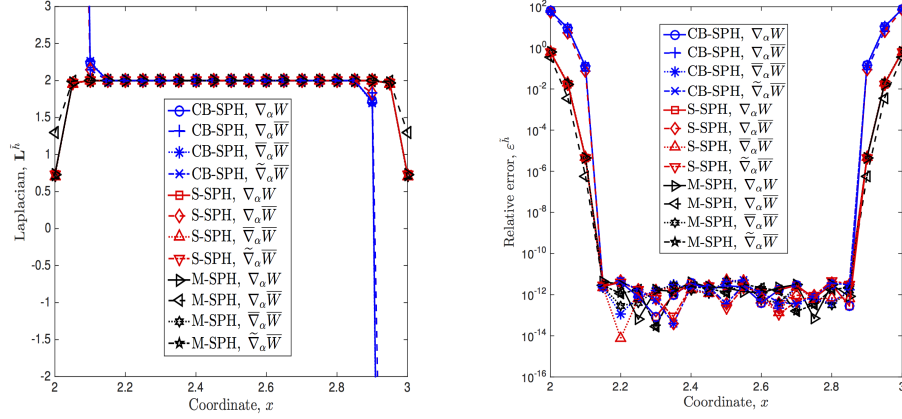
FIGURE 5. Cross-section of the test patch at $y = 2.5$. Three SPH approximations of $\nabla((x + y)(\nabla(x + y)))$ with different kernel gradients are shown. The different schemes and kernel gradients are described in the caption of Figure (3).

where τ is the iteration parameter (e.g., time step), n is the iteration index (e.g., time index), $\{\mathbf{u}\}^n = (\boldsymbol{u}_1^n, \ldots, \boldsymbol{u}_N^n)$ is a vector of all N particle values $\boldsymbol{u}_i^n$, $i = 1, \ldots, N$, $\{\boldsymbol{b}\} = (\boldsymbol{b}_1, \ldots, \boldsymbol{b}_N)$ is the right-hand side vector. The expression (52) may represent, for example, discretization of the parabolic PDE or an iterative solver of the linear system of equations arising from discretization of elliptic boundary value problem. Substituting into the left-hand side of the relation (52) the following form of perturbation

$$\boldsymbol{u}_j^n = \lambda^n e^{\mathbf{i}\boldsymbol{k}_j \cdot \boldsymbol{r}_j} = \lambda^n \cdot \prod_{l=1}^{n} e^{\mathbf{i}k_j^l \cdot x_j^l} \tag{53}$$

leads to the expression for the von Neumann growth factor subject to (52) and linear Laplace operator:

$$\lambda_j(\tau) = 1 + \tau \cdot e^{-\mathbf{i}\boldsymbol{k}_j \cdot \boldsymbol{r}_j} \cdot \mathbf{L}^{\tilde{h}}\left[\left\{e^{\mathbf{i}\boldsymbol{k} \cdot \boldsymbol{r}}\right\}\right], \boldsymbol{r} \in \mathbb{R}^n, \ n = 1, 2, 3; \tag{54}$$

where $\left\{e^{\mathbf{i}\boldsymbol{k} \cdot \boldsymbol{r}}\right\} = \left(e^{\mathbf{i}\boldsymbol{k}_1 \cdot \boldsymbol{r}_1}, \ldots, e^{\mathbf{i}\boldsymbol{k}_N \cdot \boldsymbol{r}_N}\right)$ and $\lambda_j(\tau)$ is the von Neumann growth factor. For the discretization to be stable, it is required that $|\lambda_j(\tau)| \leq 1$, $\forall j$. The von Neumann growth factor is shown for three main discretization schemes: Corrected Brookshaw's scheme (CB-SPH) (30), Schwaiger's scheme (S-SPH) (31)–(34) and new approximation (M-SPH) (44)–(46) for uniform and pseudo random particle distribution with $\tau = 0.25$ and $\mathbf{M}^{\alpha\beta}(\boldsymbol{r}) = \delta_{\alpha\beta}$ (see, Figures 7). In case of uniform particle distribution, the von Neumann growth factor clusters around the real axis for all schemes and satisfies the requirement $|\lambda_j(\tau)| \leq 1$, $\forall j$. In case of pseudo random particle distribution, the von Neumann growth factor has both real and imaginary parts forming complex shape but satisfying the requirement $|\lambda_j(\tau)| \leq 1$, $\forall j$ almost everywhere (i.e., it could be some problems at the boundary particles).

4.4. **Monotonicity and Convergence.** In real life applications, the numerical domains are large and, therefore, many degree of freedom (i.e., unknowns) is required. The resulting matrix is usually sparse, but because of fill-in a direct method requires significant amount of memory and time in general case. Hence, iterative solvers are used to overcome these issues. The iterative solvers
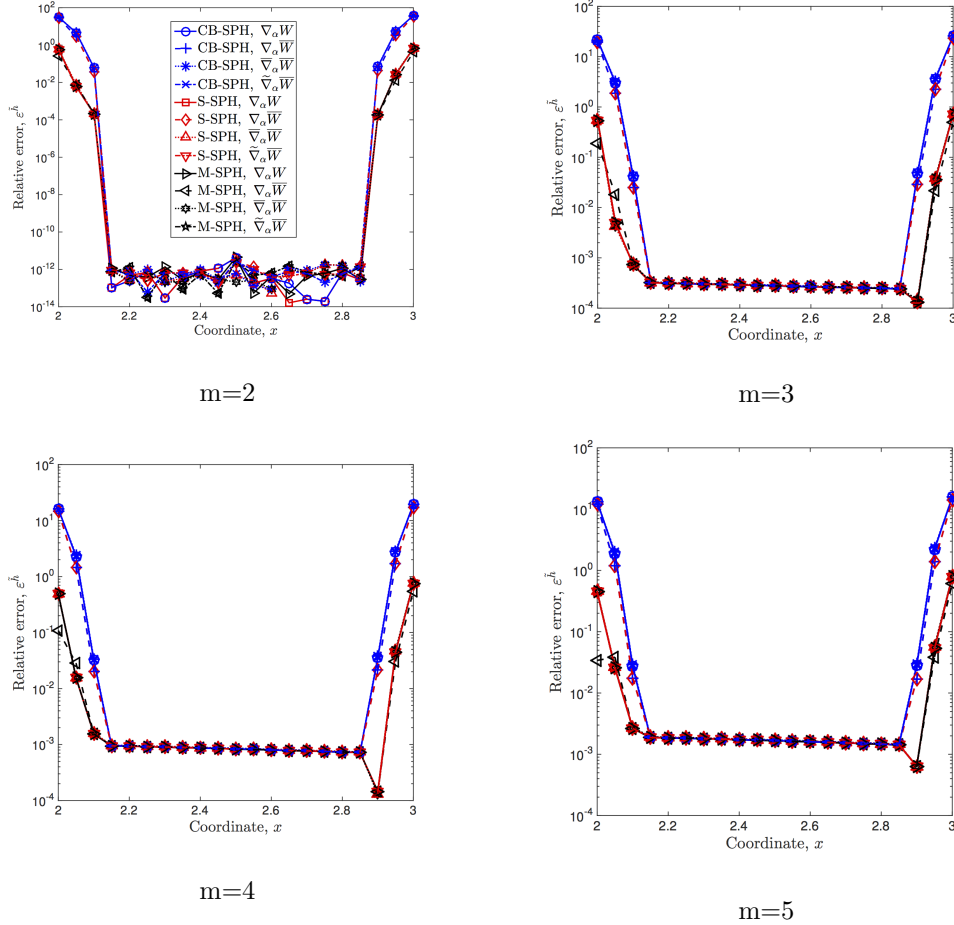
m=2

m=3

m=4

m=5

FIGURE 6. The relative errors along $y = 2.5$ for each of the discretizations used in Figure 3 are shown here only for the suite of functions $\nabla \left[(x^m + y^m) \nabla (x + y) \right]$ where $m = 2, \ldots, 5$. Four different options of computing kernel gradients (i.e., $\nabla_\gamma W$, $\nabla_\alpha \overline{W}$), and corrected kernel gradients (i.e., $\nabla_\gamma^* W$, $\nabla_\alpha^* \overline{W}$, $\overline{\nabla}_\alpha^* \overline{W}$, and $\widetilde{\nabla}_\alpha^* \overline{W}$) are shown.

converge only if the matrix satisfies certain properties related to the property of the diagonal dominance. However, these properties are only sufficient conditions for the method to converge.

The proof of the convergence of linear meshless schemes applied to a linear elliptic boundary value problem can be done in the following steps (see, Bouchon (2007) [48], Bouchon and Peichl (2007) [49], Matsunaga and Yamamoto (2000) [50], Thomée (2001) [51]: if it is shown that the truncation error ε tends to 0 as the maximum smoothing length $\max_{I \in N} h_I$ goes to 0, then the linear system $\mathbf{A} \delta u = \varepsilon$ that couples the variable error δu with ε proves the convergence of the schemes, given that the matrix of the discretized meshless operator is monotone. A square matrix $\mathbf{A} = (a_{ij})_{1 \leq i \leq n, 1 \leq j \leq n} \in \mathbb{R}^{n \times n}$ is called monotone if $a_{ij} \leq 0 \ \forall i \neq j$, $a_{ii} > 0 \ \forall i$ and it is inverse positive
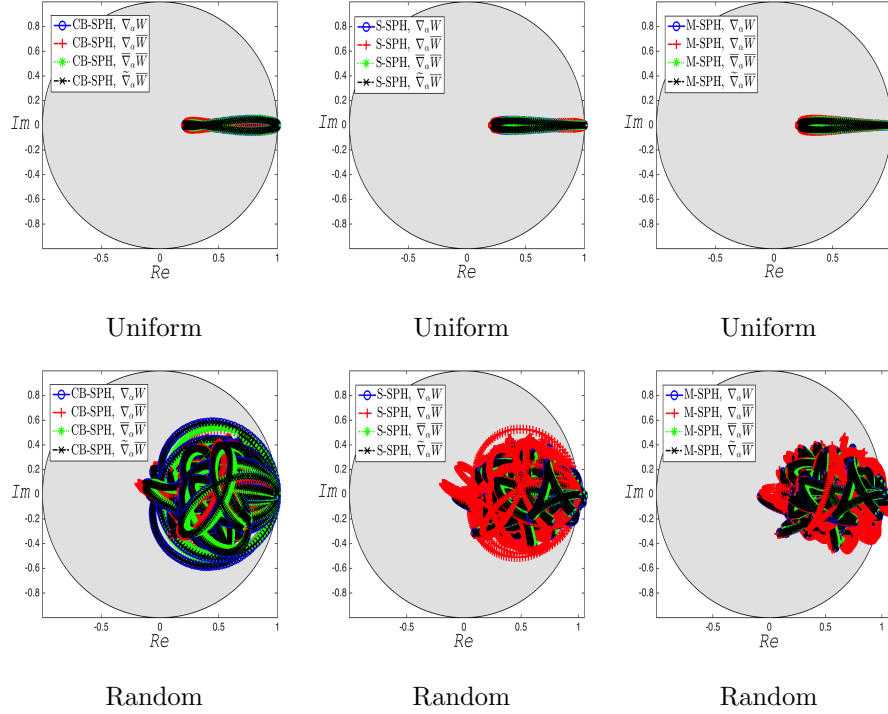
FIGURE 7. von Neumann growth factor for different discretization schemes. Corrected Brookshaw's scheme (CB-SPH) is given by (30) with the correction multiplier, while Schwaiger's scheme (S-SPH) is given by (31)–(34). New approximation (M-SPH) considered here are the SPH form (44)–(46). Four different options of computing kernel gradients (i.e., $\nabla_\gamma W$, $\nabla_\alpha \overline{W}$, and corrected kernel gradients (i.e., $\nabla_\gamma^* W$, $\nabla_\alpha^* \overline{W}$, $\overline{\nabla}_\alpha^* \overline{W}$, and $\widetilde{\nabla}_\alpha^* \overline{W}$) are shown.

$\mathbf{A}^{-1} \geq 0$. Furthermore, the monotone schemes do satisfy a discrete maximum principle producing solutions without spurious oscillations.

It is clear that the new scheme (44)–(46) can be written in the form (40), where meshless transmissibility between particles $\mathbf{r}_J$ and $\mathbf{r}_I$ can be defined as $T(\mathbf{r}_J, \mathbf{r}_I) = \dfrac{\bar{\Gamma}_{\beta\beta}}{n}(m_I + m_J) \bar{T}_{IJ}$ with:

$$\bar{T}_{IJ} = \left\{ \frac{(\mathbf{r}_J - \mathbf{r}_I) \cdot \overline{\nabla W}\left(\mathbf{r}_J - \mathbf{r}_I, \tilde{h}_{IJ}\right)}{\|\mathbf{r}_J - \mathbf{r}_I\|^2} - \overline{\nabla}_\alpha^* W\left(\mathbf{r}_J - \mathbf{r}_I, \tilde{h}_{IJ}\right) \mathbf{N}^\alpha \right\}, \tag{55}$$

where $\mathbf{N}^\alpha(\mathbf{r}_I)$ is defined by (32). This allows us to formulate the following remark.

Remark 3. *Taking into account Remark 2 and the following relation:*

$$\frac{(\mathbf{r}_J - \mathbf{r}_I) \cdot \overline{\nabla W}(\mathbf{r}_J - \mathbf{r}_I, h)}{\|\mathbf{r}_J - \mathbf{r}_I\|^2} = \frac{1}{z \cdot h^2} \frac{\overline{dW}}{dz}(z) \leq 0, \tag{56}$$

and the relation (48) *which all together lead to the fact that there is a parameter* $\tilde{h}_I$ *such that* $T(\mathbf{r}_J, \mathbf{r}_I) \geq 0$. *This means that the proposed scheme subject to this parameter* $\tilde{h}_I$ *is monotone for the medium with the scalar heterogeneous coefficients.*

5. Solution of Boundary Value Problems

Following the work by [2], the numerical tests for inhomogeneous Dirichlet, Neumann and mixed boundary conditions are considered for homogeneous and heterogeneous media with the characteristics $\mathbf{M}(\mathbf{r})$. To illustrate the performance of the proposed scheme, a modelling of a single phase steady-state fluid flow in fully anisotropic porous media with different type of boundary conditions is also presented in this section. The square 2D and 3D domains (3) are considered.

The relative error used to quantify the accuracy of the proposed schemes in the subsections (2.3), (2.4), and (3.1) during numerical simulation in this section is given by:

$$\|E_R\|_{\Omega}^{L^2} = \left[\frac{1}{\sum\limits_{\Omega} V_{\mathbf{r}_J}} \sum\limits_{\Omega} V_{\mathbf{r}_K} \left(\frac{\mathbf{u}(\mathbf{r}_K) - \langle \mathbf{u}(\mathbf{r}_K) \rangle}{\mathbf{u}(\mathbf{r}_K)} \right)^2 \right]^{1/2} \tag{57}$$

where $\mathbf{u}(\mathbf{r})$ is the analytical or reference solution field and $\langle \mathbf{u}(\mathbf{r}_K) \rangle$ is the approximated solution field. Several numerical results using considered in this paper schemes for uniform and pseudo random particle distributions are shown in the following sections that confirm the theoretical results from the previous sections.
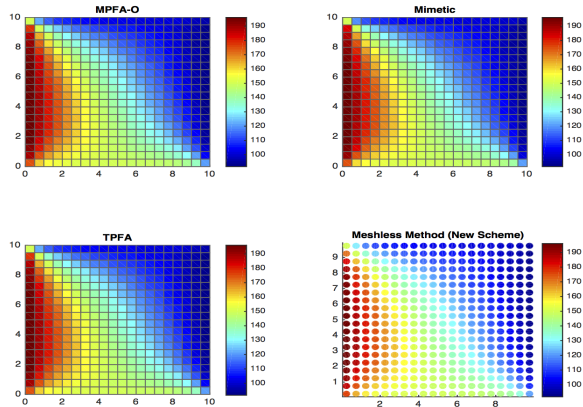

FIGURE 8. Comparison of solutions of the Dirichlet problem for the Laplace equation. The method used are MPFA-O, Mimetic, TPFA, and Meshless methods (New Method: (44)–(46)).

5.1. **Inhomogeneous Boundary Condition.** Firstly, the homogeneous properties of the porous media $\mathbf{M}(\mathbf{r}) = \mathbf{I}$ are assumed for simplicity of the derivation. The analytical solution of (1) subject

to the assumption that $g(\boldsymbol{r}) \equiv 0$ for $\boldsymbol{r} \in \Omega \subset \mathbb{R}^2$ and constant boundary conditions is the following:

$$
\begin{aligned}
\mathbf{u}(x,y) = & \sum_{n=odd} \left[\frac{4\psi_1}{n\pi \sinh\left(\frac{n\pi H}{L}\right)} \right] \sin\left(\frac{n\pi}{L}x\right) \sinh\left(\frac{n\pi}{L}(H-y)\right) + \\
& + \sum_{n=odd} \left[\frac{4\psi_2}{n\pi \sinh\left(\frac{n\pi L}{H}\right)} \right] \sin\left(\frac{n\pi}{H}y\right) \sinh\left(\frac{n\pi}{H}x\right) + \\
& + \sum_{n=odd} \left[\frac{4\psi_3}{n\pi \sinh\left(\frac{n\pi L}{H}\right)} \right] \sin\left(\frac{n\pi}{H}y\right) \sinh\left(\frac{n\pi}{H}x\right) + \\
& + \sum_{n=odd} \left[\frac{4\psi_4}{n\pi \sinh\left(\frac{n\pi L}{H}\right)} \right] \sin\left(\frac{n\pi}{H}y\right) \sinh\left(\frac{n\pi}{H}(L-x)\right),
\end{aligned}
\tag{58}
$$

where ψ_1 is the boundary at $y=0$, ψ_2 at $x=L$, ψ_3 at $y=H$, and ψ_4 at $x=0$.

Tables 1, 2 shows the convergence rate of different schemes for uniform particle distribution. The solutions with MPFA and Mimetic schemes were obtained using MATLAB Reservoir Simulation Toolbox (MRST) [52]. It is clear from the convergence results that schemes (31)–(34) and (44)–(46) are identical and they overperform the scheme (30). The convergence rate as was predicted theoretically is at least $\mathcal{O}(h^\omega)$, $1 \le \omega \le 2$. Tables 3, 4 shows the convergence rate for different

TABLE 1. The error of convergence for different schemes (uniform particle distribution) and $f = 0.5005$.

DoF	MPFA	Mimetic	Brookshaw (30)	Schwaiger (31)–(34)	New Scheme (44)–(46)
25	$1.318 \cdot 10^{-1}$	$1.240 \cdot 10^{-1}$	$1.314 \cdot 10^0$	$6.608 \cdot 10^{-2}$	$6.608 \cdot 10^{-2}$
100	$3.296 \cdot 10^{-2}$	$3.078 \cdot 10^{-2}$	$3.925 \cdot 10^{-1}$	$1.865 \cdot 10^{-2}$	$1.865 \cdot 10^{-2}$
400	$8.233 \cdot 10^{-3}$	$7.685 \cdot 10^{-3}$	$1.105 \cdot 10^{-1}$	$4.714 \cdot 10^{-3}$	$4.714 \cdot 10^{-3}$
1600	$2.058 \cdot 10^{-3}$	$1.920 \cdot 10^{-3}$	$3.025 \cdot 10^{-2}$	$1.179 \cdot 10^{-3}$	$1.179 \cdot 10^{-3}$
6400	$5.318 \cdot 10^{-4}$	$4.968 \cdot 10^{-4}$	$8.152 \cdot 10^{-3}$	$3.213 \cdot 10^{-4}$	$3.213 \cdot 10^{-4}$
25600	$3.007 \cdot 10^{-4}$	$2.955 \cdot 10^{-4}$	$2.193 \cdot 10^{-3}$	$2.807 \cdot 10^{-4}$	$2.807 \cdot 10^{-4}$

TABLE 2. The error of convergence for different schemes (uniformed particle distribution) and $f = 1.001$.

DoF	Brookshaw (30)	Schwaiger (31)–(34)	New Scheme (44)–(46)
25	$2.312 \cdot 10^{-1}$	$1.091 \cdot 10^{-1}$	$1.091 \cdot 10^{-1}$
100	$1.120 \cdot 10^{-1}$	$2.698 \cdot 10^{-2}$	$2.698 \cdot 10^{-2}$
400	$3.998 \cdot 10^{-2}$	$6.737 \cdot 10^{-3}$	$6.737 \cdot 10^{-3}$
1600	$1.262 \cdot 10^{-2}$	$1.684 \cdot 10^{-3}$	$1.684 \cdot 10^{-3}$
6400	$3.737 \cdot 10^{-3}$	$4.418 \cdot 10^{-4}$	$4.418 \cdot 10^{-4}$
25600	$1.097 \cdot 10^{-3}$	$2.919 \cdot 10^{-4}$	$2.919 \cdot 10^{-4}$

schemes and pseudo random distribution. The reason for starting from $f = 0.5005$ is that we want to force the same number of non-zero entries in the matrix as for MPFA or Memetic methods. This procedure may lead to a badly conditioned matrix since $\overline{\nabla W}\left(\boldsymbol{r}_J - \boldsymbol{r}_I, h\right) \ll 1$. This distribution of particles was generated by perturbing the regularly distributed particles using a uniform random variable varying between $+10\%$ and -10% of the maximum smoothing length $h_{max} = 1.001$. Since random realizations are used to compute errors, the statistical data about 30 realizations are used to compute mean values and standard deviations. This data is presented in Tables 3, 4. The positive trends of the scheme remain the same as for the case of uniform particle distributions. The scheme (30) has higher error compare to schemes (31)–(34) and (44)–(46). However, the dispersion of the approximation error is higher in the scheme (44)–(46). Figure 8 shows the numerical solution

TABLE 3. The error of convergence for different schemes (random particle distribution) and $f = 0.6006$.

DoF	Brookshaw (30)	Schwaiger (31)–(34)	New Scheme (44)–(46)
25	$1.102 \cdot 10^{+0} \pm 1.966 \cdot 10^{-2}$	$1.940 \cdot 10^{-1} \pm 3.954 \cdot 10^{-2}$	$3.707 \cdot 10^{-1} \pm 1.319 \cdot 10^{-1}$
100	$3.361 \cdot 10^{-1} \pm 4.923 \cdot 10^{-3}$	$5.511 \cdot 10^{-2} \pm 1.205 \cdot 10^{-2}$	$9.074 \cdot 10^{-2} \pm 2.668 \cdot 10^{-2}$
400	$9.576 \cdot 10^{-2} \pm 8.705 \cdot 10^{-4}$	$1.376 \cdot 10^{-2} \pm 2.440 \cdot 10^{-3}$	$2.299 \cdot 10^{-2} \pm 6.972 \cdot 10^{-3}$
1600	$2.640 \cdot 10^{-2} \pm 2.551 \cdot 10^{-4}$	$4.157 \cdot 10^{-3} \pm 7.485 \cdot 10^{-4}$	$5.912 \cdot 10^{-3} \pm 1.289 \cdot 10^{-3}$
6400	$7.185 \cdot 10^{-3} \pm 5.982 \cdot 10^{-5}$	$1.044 \cdot 10^{-3} \pm 1.465 \cdot 10^{-4}$	$1.406 \cdot 10^{-3} \pm 3.090 \cdot 10^{-4}$
25600	$1.944 \cdot 10^{-3} \pm 1.451 \cdot 10^{-5}$	$3.858 \cdot 10^{-4} \pm 5.887 \cdot 10^{-5}$	$4.960 \cdot 10^{-4} \pm 8.425 \cdot 10^{-5}$

TABLE 4. The error of convergence for different schemes (random particle distribution) and $f = 1.2012$.

DoF	Brookshaw (30)	Schwaiger (31)–(34)	New Scheme (44)–(46)
25	$3.578 \cdot 10^{-1} \pm 2.879 \cdot 10^{-2}$	$2.162 \cdot 10^{-1} \pm 2.800 \cdot 10^{-2}$	$1.842 \cdot 10^{-1} \pm 8.871 \cdot 10^{-3}$
100	$1.261 \cdot 10^{-1} \pm 4.859 \cdot 10^{-3}$	$5.696 \cdot 10^{-2} \pm 5.518 \cdot 10^{-3}$	$4.596 \cdot 10^{-2} \pm 1.999 \cdot 10^{-3}$
400	$4.224 \cdot 10^{-2} \pm 1.092 \cdot 10^{-3}$	$1.493 \cdot 10^{-2} \pm 1.546 \cdot 10^{-3}$	$1.157 \cdot 10^{-2} \pm 5.691 \cdot 10^{-4}$
1600	$1.299 \cdot 10^{-2} \pm 2.031 \cdot 10^{-4}$	$3.934 \cdot 10^{-3} \pm 3.969 \cdot 10^{-4}$	$2.889 \cdot 10^{-3} \pm 1.451 \cdot 10^{-4}$
6400	$3.862 \cdot 10^{-3} \pm 3.452 \cdot 10^{-5}$	$1.037 \cdot 10^{-3} \pm 8.443 \cdot 10^{-5}$	$7.507 \cdot 10^{-4} \pm 4.060 \cdot 10^{-5}$
25600	$1.133 \cdot 10^{-3} \pm 2.125 \cdot 10^{-5}$	$4.087 \cdot 10^{-4} \pm 5.405 \cdot 10^{-5}$	$3.475 \cdot 10^{-4} \pm 3.814 \cdot 10^{-5}$

of the boundary value problem obtained using different discretization methods. The solution was obtained using 40 particles/cells in each direction.

5.2. **Inhomogeneous Mixed Boundary Condition Test.** The general steady-state solution for a Dirichlet condition along the base of the plate and Neumann conditions elsewhere is given in [2] by

$$\mathbf{u}\left(x, y\right) = \psi_1 + \psi_3 y + \sum_{n=1}^{\infty} \frac{2\psi_2 \cosh\left(\lambda_n x\right) + 2\psi_4 \cosh\left(\lambda_n\left(L - x\right)\right)}{H \lambda_n^2 \sinh\left(\lambda_n L\right)} \sinh\left(\lambda_n y\right), \tag{59}$$

where ψ_1 is the boundary value of $\mathbf{u}$ at $y = 0$, ψ_2 is the flux at $x = L$, ψ_3 is the flux at $y = H$, and ψ_4 is the flux at $x = 0$, and $\lambda_n = \dfrac{\left(2n - 1\right)\pi}{2H}$. The following parameters (dimensionless)

were chosen:$\psi_1 = 150$, $\psi_3 = 150$, $\psi_4 = 200$, $\psi_2 = 90$. Again, for uniform and regular particles distribution, MPFA method reduces to the TPFA. Similar to the previous section, the regular and pseudo random particle distribution are considered to access the convergence properties of the proposed schemes.

Remark 4. *Let $\Gamma_N = \varnothing$ and $\Gamma_D = \varnothing$, $g(\boldsymbol{r}) \geq 0$, $\boldsymbol{r} \in \Omega$, $g_N(\boldsymbol{r}) \geq 0$, $\boldsymbol{r} \in \Gamma_N$, $g_D(\boldsymbol{r}) \geq 0$, $\boldsymbol{r} \in \Gamma_D$ and the solution of*

$$\mathbf{L}(\mathbf{u}) = 0, \quad or \quad \nabla(\mathbf{M}(\boldsymbol{r})\nabla \mathbf{u}(\boldsymbol{r})) = g(\boldsymbol{r}), \ \ \forall \boldsymbol{r} \in \Omega \subset \mathbb{R}^n, \tag{60}$$

exists then it can be discretized in all internal particles by the following schemes Brookshaw (30), Schwaiger (31)–(34), and New Scheme (44)–(46) and compounded with the following condition for all $\boldsymbol{r} \in \Gamma_N$:

$$\langle \boldsymbol{u}^\alpha \boldsymbol{n}_\alpha \rangle = \boldsymbol{n}_\alpha \mathbf{M}^{\alpha\beta}(\boldsymbol{r}) \sum_{\Omega_{\boldsymbol{r},\bar{h}}} V_{\boldsymbol{r}_J} \left[\mathbf{u}(\boldsymbol{r}_J) - \mathbf{u}(\boldsymbol{r}_I) \right] \overline{\nabla_\beta^* W}(\boldsymbol{r}_J - \boldsymbol{r}_I, h) \tag{61}$$

where $\boldsymbol{n}_\alpha$ are the component of the external normal to the boundary $\boldsymbol{r} \in \Gamma_N$.

The following smoothing multiplication factors $f = 0.5005$, $f = 1.001$, and $f = 2.002$ are considered. Tables 5, 6 show the convergence rate for different schemes using the uniform and pseudo random particle distribution. The convergence rate as was predicted theoretically is at least $\mathcal{O}(h^\omega)$, $1 \leq \omega < 2$. Interestingly, the scheme (30) shows a very bad convergence rate for $f = 0.5005$. This explains by the fact that we have one particle from each side in the kernel support almost next to the boundary of the kernel support leading to $\overline{\nabla W}(\boldsymbol{r}_J - \boldsymbol{r}_I, h) \ll 1$ and, hence, to a badly conditioned matrix. This does not observed for other schemes due to the normalization coefficient. As a result, the scheme (30) should be used with more than one particle in the compact support in each direction leading to a larger bandwidth in the matrix.

TABLE 5. The error of convergence for different schemes (uniform particle distribution) and $f = 0.5005$.

DoF	MPFA	Mimetic	Brookshaw (30)	Schwaiger (31)–(34)	New Scheme (44)–(46)
25	$1.489 \cdot 10^{-1}$	$2.651 \cdot 10^{-2}$	$1.489 \cdot 10^{6}$	$8.244 \cdot 10^{-1}$	$8.244 \cdot 10^{-1}$
100	$2.015 \cdot 10^{-2}$	$4.424 \cdot 10^{-3}$	$9.471 \cdot 10^{5}$	$2.178 \cdot 10^{-1}$	$2.178 \cdot 10^{-1}$
400	$2.727 \cdot 10^{-3}$	$6.889 \cdot 10^{-4}$	$5.378 \cdot 10^{5}$	$5.550 \cdot 10^{-2}$	$5.550 \cdot 10^{-2}$
1600	$3.666 \cdot 10^{-4}$	$1.024 \cdot 10^{-4}$	$2.859 \cdot 10^{5}$	$1.398 \cdot 10^{-2}$	$1.398 \cdot 10^{-2}$
6400	$4.951 \cdot 10^{-5}$	$1.522 \cdot 10^{-5}$	$1.473 \cdot 10^{5}$	$3.504 \cdot 10^{-3}$	$3.504 \cdot 10^{-3}$
25600	$7.309 \cdot 10^{-6}$	$2.920 \cdot 10^{-6}$	$7.474 \cdot 10^{4}$	$8.770 \cdot 10^{-4}$	$8.770 \cdot 10^{-4}$

Tables 7, 8 show the convergence rate for different schemes with pseudo random particle distribution. The pseudo random distribution of particles was again generated by perturbing the regularly distributed particles using the uniform random variable varying between $+10\%$ and -10% of the maximum smoothing length $h_{max} = 1.001$. Similar to the above case, the statistical data about 30 realizations are used to compute mean values and standard deviations. These data are presented in Tables 7, 8. The general trends of the scheme prosperities remain the same as for uniform particle distributions. The scheme (30) has higher error compared to schemes (31)–(34) and (44)–(46). However, the dispersion of the approximation error is higher in the scheme (44)–(46). Results of the numerical solution are compared with the series solution in Figure 11.

TABLE 6. The error of convergence for different schemes (uniform particle distribution) and $f = 1.001$.

DoF	Brookshaw (30)	Schwaiger (31)–(34)	New Scheme (44)–(46)
25	$1.163 \cdot 10^0$	$1.078 \cdot 10^{-1}$	$1.078 \cdot 10^{-1}$
100	$1.208 \cdot 10^0$	$1.488 \cdot 10^{-2}$	$1.488 \cdot 10^{-2}$
400	$8.291 \cdot 10^{-1}$	$2.244 \cdot 10^{-3}$	$2.244 \cdot 10^{-3}$
1600	$4.831 \cdot 10^{-1}$	$4.215 \cdot 10^{-4}$	$4.215 \cdot 10^{-4}$
6400	$2.606 \cdot 10^{-1}$	$9.858 \cdot 10^{-5}$	$9.858 \cdot 10^{-5}$
25600	$1.353 \cdot 10^{-1}$	$2.502 \cdot 10^{-5}$	$2.502 \cdot 10^{-5}$

TABLE 7. The error of convergence for different schemes (random particle distribution) and $f = 0.6006$.

DoF	Brookshaw (30)	Schwaiger (31)–(34)	New Scheme (44)–(46)
25	$5.608 \cdot 10^1 \pm 1.019 \cdot 10^0$	$8.815 \cdot 10^{-1} \pm 4.248 \cdot 10^{-1}$	$1.242 \cdot 10^0 \pm 5.058 \cdot 10^{-1}$
100	$3.769 \cdot 10^1 \pm 5.708 \cdot 10^{-1}$	$3.454 \cdot 10^{-1} \pm 1.977 \cdot 10^{-1}$	$4.361 \cdot 10^{-1} \pm 2.425 \cdot 10^{-1}$
400	$2.154 \cdot 10^1 \pm 1.757 \cdot 10^{-1}$	$8.454 \cdot 10^{-2} \pm 5.111 \cdot 10^{-2}$	$1.525 \cdot 10^{-1} \pm 1.195 \cdot 10^{-1}$
1600	$1.159 \cdot 10^1 \pm 7.457 \cdot 10^{-2}$	$2.245 \cdot 10^{-2} \pm 1.055 \cdot 10^{-2}$	$4.563 \cdot 10^{-2} \pm 2.328 \cdot 10^{-2}$
6400	$6.027 \cdot 10^0 \pm 2.312 \cdot 10^{-2}$	$1.104 \cdot 10^{-2} \pm 7.523 \cdot 10^{-3}$	$1.848 \cdot 10^{-2} \pm 9.276 \cdot 10^{-3}$
25600	$3.054 \cdot 10^0 \pm 1.174 \cdot 10^{-2}$	$4.123 \cdot 10^{-3} \pm 2.059 \cdot 10^{-3}$	$5.879 \cdot 10^{-3} \pm 4.253 \cdot 10^{-3}$

TABLE 8. The error of convergence for different schemes (random particle distribution) and $f = 1.2012$.

DoF	Brookshaw (30)	Schwaiger (31)–(34)	New Scheme (44)–(46)
25	$5.177 \cdot 10^{-1} \pm 7.312 \cdot 10^{-2}$	$3.143 \cdot 10^{-1} \pm 7.543 \cdot 10^{-2}$	$4.302 \cdot 10^{-1} \pm 1.461 \cdot 10^{-1}$
100	$5.160 \cdot 10^{-1} \pm 4.035 \cdot 10^{-2}$	$5.959 \cdot 10^{-2} \pm 4.713 \cdot 10^{-3}$	$1.106 \cdot 10^{-1} \pm 1.739 \cdot 10^{-2}$
400	$4.349 \cdot 10^{-1} \pm 1.715 \cdot 10^{-2}$	$1.515 \cdot 10^{-2} \pm 1.973 \cdot 10^{-3}$	$3.015 \cdot 10^{-2} \pm 1.045 \cdot 10^{-2}$
1600	$2.745 \cdot 10^{-1} \pm 9.059 \cdot 10^{-3}$	$3.926 \cdot 10^{-3} \pm 6.865 \cdot 10^{-4}$	$1.133 \cdot 10^{-2} \pm 5.486 \cdot 10^{-3}$
6400	$1.508 \cdot 10^{-1} \pm 2.822 \cdot 10^{-3}$	$1.595 \cdot 10^{-3} \pm 8.144 \cdot 10^{-4}$	$3.187 \cdot 10^{-3} \pm 1.438 \cdot 10^{-3}$
25600	$7.958 \cdot 10^{-2} \pm 1.146 \cdot 10^{-3}$	$5.354 \cdot 10^{-4} \pm 2.036 \cdot 10^{-4}$	$9.201 \cdot 10^{-4} \pm 5.201 \cdot 10^{-4}$

5.3. **SPE10.** In addition, we investigate the accuracy of the numerical schemes using a well-known SPE10 benchmark [53] with the Laplace equation:

$$
\begin{aligned}
&\mathbf{L}\left(\mathbf{u}\right) = -\nabla\left(\mathbf{M}\left(\boldsymbol{r}\right)\nabla\mathbf{u}\left(\boldsymbol{r}\right)\right) = 0, \ \forall \boldsymbol{r} \in \Omega \subset \mathbb{R}^n, \\
&\mathbf{M}^{\alpha\beta}\left(\boldsymbol{r}\right) = K^{\alpha\beta}\left(\boldsymbol{r}\right), \ K^{\alpha\beta}\left(\boldsymbol{r}\right) = 0 \ \forall \alpha \neq \beta; \ \alpha, \beta = 1, \ldots, n;
\end{aligned}
\tag{62}
$$

where $\mathbf{u}\left(\boldsymbol{r}\right)$ is the unknown pressure field, $K^{\alpha\beta}\left(\boldsymbol{r}\right)$ is the diagonal permeability field. The original model contains 85 layers, where layers from 1 to 35 have smooth permeability with lognormal distribution and layers 36 to 85 have channelized formations that are considered to be significantly more challenging for numerical simulations. The subset of this model is defined by the global
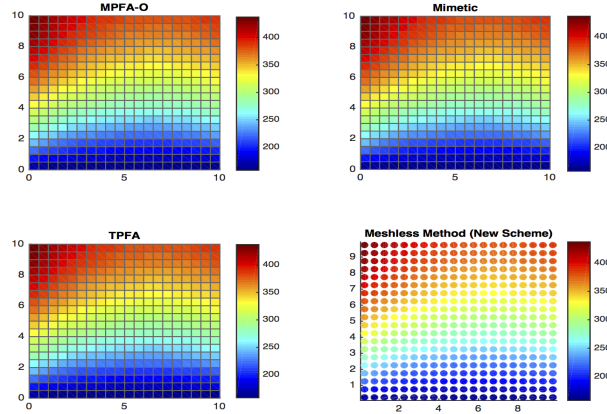
FIGURE 9. Comparison of solutions of the inhomogeneous mixed boundary problems for the Laplace equations. The method used are MPFA-O, Mimetic, TPFA, and Meshless methods (New Method: (44)–(46)).
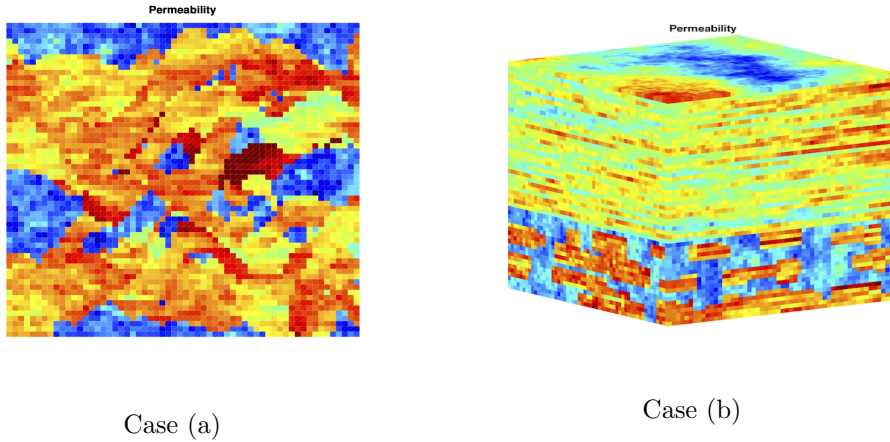

Case (a)

Case (b)

FIGURE 10. The lognormal permeability field in the SPE10 benchmark test. Case (a) 60×60cells of 85 layer. Case (b) subsection of the SPE10 model defined by $60 \times 60 \times 60$ cells.

Cartesian indices I, J, K. The 85 layer was used as a permeability field for 2D simulation with Cartesian indices $I = 1 : 60$ and $J = 1 : 60$. In 3D, the subsection Cartesian indices $I = 1 : 60$, $J = 1 : 60$, and $K = 1 : 60$. The permeability fields K^{11} for both cases are shown in Figure 10. The boundary conditions correspond to the unit pressure drop over the entire domain in J-direction (i.e., $y_{min} = 0$ and $y_{max} = 1$). The numerical results using new scheme for the SPE10 cases are presented in Figure 11. The relative error distribution is also shown for 2D and 3D cases, where the error is computed using (57) and numerical solution based on TPFA. Figures 12 and 13 compare the

Numerical Solution (2D Case)   Relative Error % (2D Case)

Numerical Solution (3D Case)   Relative Error % (3D Case)
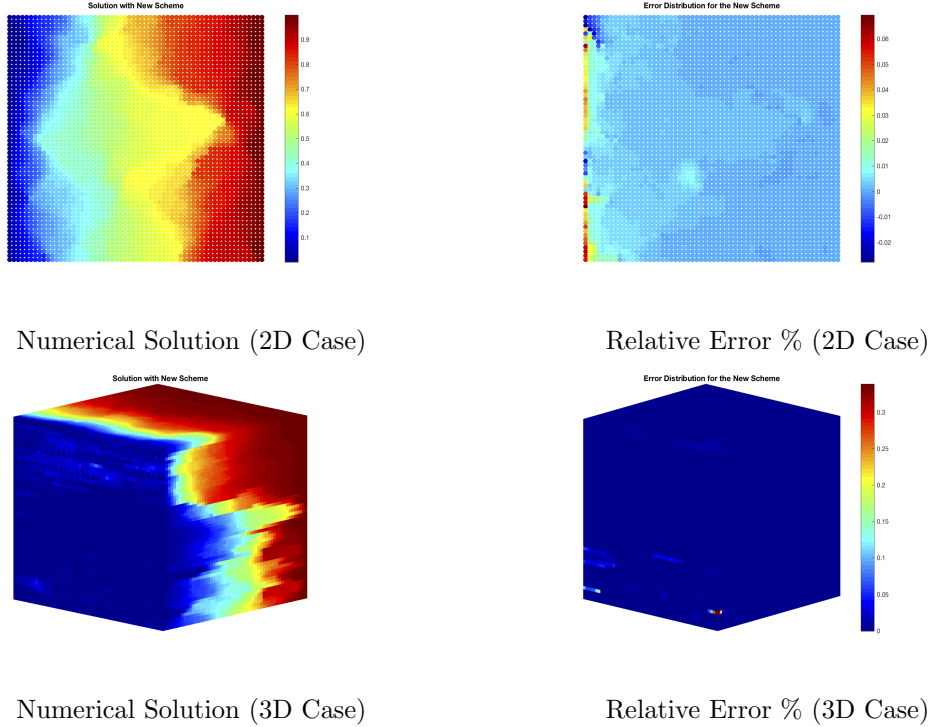
FIGURE 11. Numerical solution obtained with the new scheme for the SPE10 cases. The relative error distribution is also shown for 2D and 3D cases, where error is computed using (57) and numerical solution based on TPFA.

convergence rates of the various discretizations subject to different preconditioners. Furthermore, if we notice the convergence comparison for this test in Figures 12 and 13, the proposed new method offers similar convergence as compared to the Schwaiger's scheme (31)–(34)). The reason for such convergence is the similarity between condition numbers of the linear system of equations resulting from these methods.

Another interesting observation in this numerical test is the small values of the relative error between the TPFA solution and proposed new method for both 2D and 3D cases. This observation exhibits the efficiency of the proposed meshless discretization scheme, which explains the higher accuracy of linear reproduction.

6. CONCLUSION

In this paper, the new stable SPH discretization of the elliptic operator for heterogeneous media is proposed. The scheme has the two-point flux approximation nature and can be written in the form of (2). Using this structure, it was possible to make some theoretical monotonicity analysis (see, Remarks 2 and 3), which is difficult to perform for other schemes (e.g., Schwaiger's method). Furthermore, it follows from the Taylor's series analysis that proposed scheme is the optimum one in this class (2) for a diagonal matrix of the operator coefficients. In addition, the proposed scheme allows to apply upwinding strategy during the solution of nonlinear PDEs.
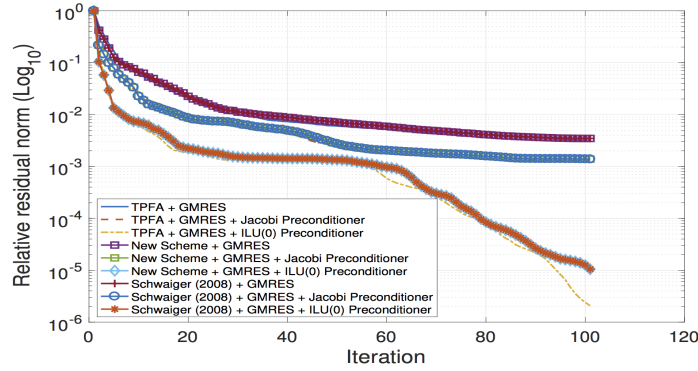
FIGURE 12. Comparison of the convergence rate of the GMRES iterative method with and without preconditioner for different numerical discretization methods (TPFA, New Scheme (44)–(46), Schwaiger (31)–(34)). The linear system of equations is built using 2D case.
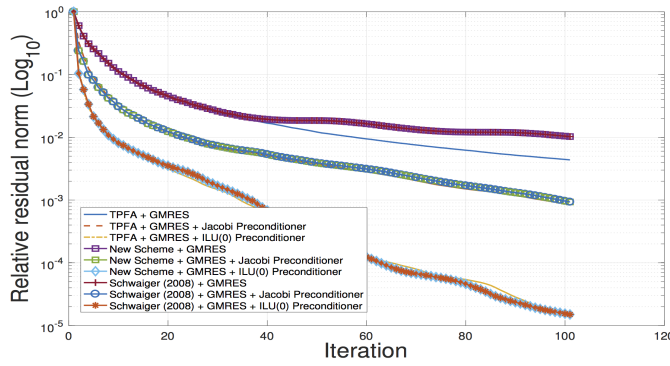

FIGURE 13. Comparison of the convergence rate of the GMRES iterative method with and without preconditioner for different numerical discretization methods (TPFA, New Scheme (44)–(46), Schwaiger (31)–(34)). The linear system of equations is built using 3D case.

The new scheme is based on a gradient approximation commonly used in thermal, viscous, and pressure projection problems and can be extended to include higher-order terms in the appropriate Taylor series. The proposed new scheme is combined with mixed corrections which ensure linear completeness. The mixed correction utilizes Shepard Functions in combination with a correction to derivative approximations. Incompleteness of the kernel support combined with the lack of consistency of the kernel interpolation in conventional meshless method results in fuzzy boundaries. In the presented meshless method, the domain boundary conditions and internal field variables are approximated with the default accuracy of the method. The resulting new scheme not only ensures first order accuracy $\mathcal{O}(h^{\alpha})$, $1 \leq \alpha \leq 2$, where h denotes the maximum particle spacing, but also minimize the impact of the particle deficiency (kernel support incompleteness) problem.

Furthermore, different Kernel gradients and their impact on the property of the scheme and accuracy are discussed. The model was tested by solving an inhomogeneous Dirichlet and mixed boundary value problems for the Laplacian equation with good accuracy confirming our theoretical results. The accuracy of Schwaiger's scheme and new scheme is the same for homogeneous particle distribution and different for the distorted particles. The new scheme takes into account all terms related to Hessian of the unknown function (see, relation (43)).

The stability analysis shows that von Neumann growth factor has both real and imaginary parts forming complex shape for general particle distribution but satisfying the stability requirement almost everywhere. The paper also discusses the monotonicity and convergence properties of the new proposed scheme and demonstrates that there is a parameter h such that the proposed new scheme is unconditionally monotone with the scalar heterogeneous media.

As was previously mentioned in the introduction, several methods have been proposed to address the difficulties involved in calculating second-order derivatives with SPH. In contrast to the present formulation, many of these methods achieve a high accuracy through fully calculating the Hessian or requiring that the discrete equations exactly reproduce quadratic functions. The primary attraction of the present method is that it provides a weak formulation for Darcy's law which can be of use in further development of meshless methods. The SPH model was previously used to model three-dimensional miscible flow and transport in porous media with complex geometry, and we are planning to use this model in future work for large (field) scale simulation of transport in porous media with general permeability distributions.

References

[1] L. Brookshaw. A method of calculating radiative heat diffusion in particle simulations. *Proceedings of the Astronomical Society of Australia*, 6(2):207–210, 1985.

[2] H.F. Schwaiger. An implicit corrected sph formulation for thermal diffusion with linear free surface boundary conditions. *International Journal for Numerical Methods in Engineering*, 75(6):647–671, 2008.

[3] L. Lucy. A numerical approach to testing the fission hypothesis. *The Astronomical Journal*, 82(12):1013–1024, 1977.

[4] R.A. Gingold and J.J. Monaghan. Smoothed particle hydrodynamics: theory and applications to non-spherical stars. *Mon. Not. R. Astr. Soc.*, 181:375–389, 1977.

[5] R.A. Gingold and J.J. Monaghan. Kernel estimates as a basis for general particle methods in hydrodynamics. *J. Comput. Phys.*, 46(3):429–453, 1982.

[6] J.J. Monaghan. Smoothed particle hydrodynamics. *Annual Reviews in Astronomy and Astrophysics*, 30:543–574, 1992.

[7] T. Belytschko, Y. Krongauz, J. Dolbow, and C. Gerlach. On the completeness of meshfree particle methods. *Int. J. for Numerical Methods in Engineering*, 43(5):785–819, 1998.

[8] J.W. Swegle, D.L. Hicks, and S.W. Attaway. Smoothed Particle Hydrodynamics stability analysis. *J. Computational Physics*, 116(1):123–134, 1995.

[9] T. Belytschko, Y. Guo, W.K. Liu, and S.P. Xiao. A unified stability analysis of meshless particle methods. *Int. J. Numer. Meth. in Engng*, 48(9):1359–1400, 2000.

[10] Ch. Zhang, X.Y. Hu, and N.A. Adams. A generalized transport-velocity formulation for smoothed particle hydrodynamics. *Journal of Computational Physics*, 337:216–232, 2017.

[11] A. Khayyer, H. Gotoh, and Y. Shimizu. Comparative study on accuracy and conservation properties of two particle regularization schemes and proposal of an optimized particle shifting scheme in isph context. *Journal of Computational Physics*, 332:236–256, 2017.

[12] M.B. Liu, G.R. Liu, and K.Y. Lam. Computer simulation of high explosive explosion using smoothed particle hydrodynamics methodology. *Comput. Fluids*, 32(3):305–322, 2003.

[13] A.A. Lukyanov. Numerical modelling of the material failure under shock loading using particle method. *Izvetiya Tula State University. Estestvennonauchn. Ser.*, 1:54–65, 2007.

[14] A.A. Lukyanov and V.B. Penkov. Numerical simulation of solids deformation by a meshless method. *Vestn. Samar. Gos. Univ. Estestvennonauchn. Ser.*, 6(56):62–70, 2007.

[15] J.J. Monaghan. Simulating free surface flows with SPH. *Journal of Computational Physics*, 110(2):399–406, 1994.

[16] G.R. Johnson, R.A. Stryk, and S.R. Beissel. SPH for high velocity impact computations. *Computational Methods in Applied Mechanical Engineering*, 139(1):347–373, 1996.

[17] J.K. Chen, J.E. Beraun, and C.J. Jih. Completeness of corrective smoothed particle method for linear elastodynamics. *Computational Mechanics*, 24(4):273–285, 1999.

[18] J.K. Chen, J.E. Beraun, and C.J. Jih. A corrective smoothed particle method for transient elastoplastic dynamics. *Computational Mechanics*, 27(3):177–187, 2001.

[19] J.P. Morris, P.J. Fox, and Y. Zhu. Modeling low Reynolds number incompressible flows using SPH. *J. Comput. Phys.*, 136(1):214–226, 1997.

[20] D.W. Holmes, J.R. Williams, and P. Tilke. Smooth particle hydrodynamics simulations of low Reynolds number flows through porous media. *International Journal for Numerical and Analytical Methods in Geomechanics*, 35(4):419–437, 2010.

[21] Y. Zhu, P.J. Fox, and J.P. Morris. A pore-scale numerical model for flow through porous media. *Int. J. Numer. Anal. Meth. Geomech.*, 23(9):881–904, 1999.

[22] Y. Zhu and P.J. Fox. Smoothed particle hydrodynamics model for diffusion through porous media. *Transport Porous Media*, 43(3):441–471, 2001.

[23] A.K. Chaniotis, D. Poulikakos, and P. Koumoutsakos. Remeshed smoothed particle hydrodynamics for the simulation of viscous and heat conduction flows. *Journal of Computational Physics*, 182(1):67–90, 2002.

[24] D.A. Fulk and D.W. Quinn. An analysis of 1-d Smoothed Particle Hydrodynamics kernels. *J. of Computational Physics*, 126(1):165–180, 1996.

[25] G.R. Liu and M.B. Liu. *Smoothed Particle Hydrodynamics: A Meshfree Particle Method*. World Scientific Publishing Co. Pte. Ltd., 2003.

[26] S. Li and W.K. Liu. Meshfree and particle methods and their applications. *Applied Mechanics Review*, 55(1):1–34, 2002.

[27] P. Breitkopf and A. Huerta. *Meshless & Particle Based Approaches in Computational Mechanics*. ISTE Publishing Company, 2004.

[28] P. Randles and L. Libersky. Smoothed Particle Hydrodynamics: Some recent improvements and applications. *Computational Methods in Applied Mechanical Engineering*, 139(1-4):375–408, 1996.

[29] S. Marrone, A. Colagrossi, D. Le Touzé, and G. Graziani. Fast free-surface detection and level-set function definition in SPH solvers. *Journal of Computational Physics*, 229(10):3652–3663, 2010.

[30] J.K. Chen, J.E. Beraun, and T.C. Carney. A corrective smoothed particle method for boundary value problems in heat conduction. *Int. J. for Numerical Methods in Engineering*, 46(2):231–252, 1999.

[31] J.K. Chen, J.E. Beraun, and C.J. Jih. An improvement for tensile instability in smoothed particle hydrodynamics. *Computational Mechanics*, 23(4):279–287, 1999.

[32] J. Bonet and S. Kulasegaram. Correction and stabilization of smooth particle hydrodynamics methods with applications in metal forming simulations. *International Journal for Numerical Methods in Engineering*, 47(6):1189–1214, 2000.

[33] F. Colin, R. Egli, and F.Y. Lin. Computing a null divergence velocity field using smoothed particle hydrodynamics. *Journal of Computational Physics*, 217(2):680–692, 2006.

[34] P.W. Cleary and J.J. Monaghan. Conduction modelling using smoothed particle hydrodynamics. *J. Comput. Phys.*, 148(1):227—264, 1999.

[35] M. Jubelgas, V. Springel, and K. Dolag. Thermal conduction in cosmological SPH simulations. *Monthly Notices of the Royal Astronomical Society*, 351(2):423–435, 2004.

[36] S.J. Cummins and M. Rudman. An SPH projection method. *Journal of Computational Physics*, 152(2):584–607, 1999.

[37] E.S. Lee, C. Moulinec, R. Xu, D. Violeau, D. Laurence, and P. Stansby. Comparison of weakly compressible and truly incompressible algorithms for the SPH mesh free particle method. *J. Comput. Phys.*, 227(18):8417–8436, 2008.

[38] X.Y. Hu and N.A. Adams. A multi-phase SPH method for macroscopic and mesoscopic flows. *J. Comput. Phys.*, 213(2):844–861, 2006.

[39] S. Zhang, S. Kuwabara, T. Suzuki, Y. Kawano, K. Morita, and K. Fukuda. Simulation of solid-fluid mixture flow using moving particle methods. *J. Comput. Phys.*, 228(7):2552–2565, 2009.

[40] W. Pan, K. Kim, M. Perego, A.M. Tartakovsky, and M.L. Parks. Modeling electrokinetic flows by consistent implicit incompressible smoothed particle hydrodynamics. *Journal of Computational Physics*, 334:125–144, 2017.

[41] J. Fang and A. Parriaux. A regularized lagrangian finite point method for the simulation of incompressible viscous flows. *J. of Computational Physics*, 227(20):8894–8908, 2008.

[42] J. Bonet and T.S.L. Lok. Variational and momentum preservation aspects of Smoothed Particle Hydrodynamic formulations. *Comput. Methods Appl. Mech. Engrg.*, 180(1-2):97–115, 1999.

[43] W.K. Liu, S. Jun, and F. Zhang. Reproducing kernel particle methods. *International Journal for Numerical Methods in Fluids*, 20(8-9):1081–1106, 1995.

[44] W.K. Liu and S. Jun. Multiple-scale reproducing kernel particle method for large deformation problems. *International Journal for Numerical Methods in Engineering*, 41(7):1339–1362, 1998.

[45] A. A. Lukyanov and C. Vuik. *Meshfree Methods for Partial Differential Equations*, chapter Meshless Multi-Point Flux Approximation, pages 67–84. 2017.

[46] S.A. Silling. Reformulation of elasticity theory for discontinuities and long-range forces. *J. Mech. Phys. Solids*, 48(1):175–209, 2000.

[47] A. Katiyar, J.T. Foster, H. Ouchi, and M.M. Sharma. A peridynamic formulation of pressure driven convective fluid transport in porous media transport in porous media. *Journal of Computational Physics*, 261:209–229, 2014.

[48] F. Bouchon. Monotonicity of some perturbations of irreducibly diagonally dominant M-matrices. *Numer. Math.*, 105(4):591–601, 2007.

[49] F. Bouchon and G.H. Peichl. A second order immersed interface technique for an elliptic Neumann problem. *Numer. Methods PDE*, 23(2):400–420, 2007.

[50] N. Matsunaga and T. Yamamoto. Superconvergence of the shortley–weller approximation for dirichlet problems. *J. Comp. Appl. Math.*, 116(2):263–273, 2000.

[51] N. Matsunaga and T. Yamamoto. From finite differences to finite elements. A short history of numerical analysis of partial differential equations. *J. Comp. Appl. Math.*, 128(1-2):1–54, 2001.

[52] K.-A. Lie. *An introduction to reservoir simulation using matlab: user guide for the matlab reservoir simulation toolbox (MRST)*. SINTEF ICT, 2016.

[53] M. A. Christie and M. J. Blunt. Tenth spe comparative solution project: A comparison of upscaling techniques. *SPE 66599, presented at the SPE Symposium on Reservoir Simulation, Houston*, 2001.